Analog Black Holes and Energy Extraction by Super-Radiance from a Single Vortex in Bose Einstein Condensates (BEC)

by

Betül Demirkaya

A Dissertation Submitted to the
Graduate School of Sciences and Engineering
in Partial Fulfillment of the Requirements for
the Degree of

Doctor of Philosophy

in

Physics

KOÇ UNIVERSITY

2019

Analog Black Holes and Energy Extraction by Super-Radiance from a Single Vortex in Bose Einstein Condensates (BEC)

Koç University

Graduate School of Sciences and Engineering

This is to certify that I have examined this copy of a doctoral dissertation by

Betül Demirkaya

and have found that it is complete and satisfactory in all respects,

and that any and all revisions required by the final

examining committee have been made.

Committee Members:

Prof. Tekin Dereli

Assoc. Prof. Kaan Güven

Prof. Ayşe Hümeyra Bilge

Prof. Özgür Müstecaplıoğlu

Assoc. Prof. Mehmet Özgür Oktel

Prof. Metin Muradoğlu

Date:

To my sister,

Esra Nur Demirkaya

ABSTRACT

Analog models of gravity, in this case, the acoustic black holes, are based on the mathematical correspondence between the propagation of sound waves in a certain media and the propagation of fields in curved spacetime. Since the direct observation of certain phenomena arising from curved space-time, such as the Hawking radiation and the superradiance, is highly impractical, analog models provide an accessible and controllable way to investigate them in the laboratory. Bose-Einstein condensate provides a convenient system for the implementation of this analogy. Indeed, the propagation of acoustic perturbations in the velocity potential of a Bose-Einstein condensate (BEC) behaves like minimally coupled massless scalar fields in a curved (2+1) dimensional Lorentzian space-time, where their propagation is governed by the Klein-Gordon wave equation. For linearized perturbations, this geometric picture can still apply in the presence of a single vortex state of the BEC. Based on this setting, this thesis work investigates the amplified scattering of axisymmetric perturbations from a vortex, as a manifestation of the acoustic superradiance. We first employ the widely used constant background density under the hydrodynamic approximation and conduct a comparative analysis of the time-domain and asymptotic frequency-domain analysis of acoustic superradiance as a function of the rotational speed of the vortex and the frequency of the impinging fluctuations. This shows that the solutions in both domains are in good agreement near the characteristic rotational speed of the single quantized vortex in its lowest energy state. However, for larger rotational speeds time-domain calculations, especially near the event horizon becomes unreliable, shown by the constraint equations introduced by the excision technique. While the simulations in frequency domain do not suffer from the numerical instabilities due to the coordinate transformations, allowing to increase the rotational velocity of the

fluid. In addition, the formulation predicts an upper bound of the reflection coefficient against the rotational velocity of the vortex.

The second part of the thesis examines the validity of the constant background density approximation by calculating a self-consistent density profile through the Gross-Pitaevskii equation. The resulting radial density profile around the vortex implies a radially varying speed of sound, which modifies the entire propagation dynamics as well as the loci of the event horizon and the ergosphere. The main conclusions of this part are that the self-consistent density profile remedies the overshoot of the superradiance dynamics temporally and that the spectral profile of the superradiance differs significantly in the vortex-scaled low frequency regime between the constant density and self-consistent density formulations. In this thesis, the superradiance phenomena for a single vortex in Bose Einstein condensate under the hydrodynamic approximation is analyzed, showing that the self-consistent density profile of the condensate improves on the constant background density approximation, particularly at the low frequency regime of acoustic perturbations. And the qualitative corrections in the transient behavior of the scattered waves energy within the ergosphere justifies the radially varying density. The analysis could be extended for external confining potentials which may be more attainable in terms of the experimental aspects of the study. In reality, setting up a BEC vortex with a drain in (2+1)-dimension may be a difficult task to achieve, acoustic black holes in BEC are already observed for a 1D-flow within a steplike potential combined with a harmonic potential.

ÖZETÇE

Analog kütleçekim modelleri, yani akustik karadelikler; belirli bazı akışkanlarda ses dalgalarının yayılımı ile eğrilikli uzay-zamanlarda ışığın yayılımı arasındaki matematiksel benzerliklere dayanmaktadır. Bu matematiksel benzerlikler, karadeliklerin Hawking ışıması veya süper-ışıması gibi uzay-zaman eğriliğinden kaynaklanan ve doğrudan gözlemlenemeyen fiziksel niteliklerinin laboratuvar ortamında kontrollü biçimde ele alınabilmesine olanak vermektedir. Özellikle Bose-Einstein yoğunlaşmaları bu tür benzerliklerinin kurulması için elverişli sistemlerdir. Bu tez çalışmasında önce bir Bose-Einstein yoğuşumunda hız potansiyelindeki pertürbasyonların yayılma hızının, kütlesiz bir skalar alanın (2+1) boyutlu eğrilikli uzay-zamanda sağladığı Klein-Gordon dalga denklemine denk olduğunu gösterilmektedir. Bu geometrik nitelik lineer pertürbasyonlar için Bose-Einstein yoğuşumunda tek-vorteks durumlarının varlığı halinde bile geçerli olmaktadır. Bu sistemlerde akustik süper-ışımanın bir görünümü olarak eksenel-simetrik pertürbasyonların tek-vortekslerden saçılırken genliklerinin yükselimi iki farklı yoğunluk dağılımı yardımıyla incelenmiştir. İlk olarak sabit hızla dönen bir vorteksi bulunan Bose-Einstein yoğuşumu için hidrodinamik yaklaşıklıkta sabit yoğunluk dağılımı ele alınmıştır. Etkiler vorteksin açısal dönme hızı ile yollanan salınımların frekansına bağlı olarak zaman-aralıklarında ve asimptotik frekans-aralıklarında karşılaştırılmalı olarak incelenmiştir. İkinci olarak, aynı konfigürasyonda yine aynı yaklaşıklıkta sınırsız bir Bose-Einstein yoğuşumunun sağlayacağı Gross-Pitaevskii denklemi çözülerek elde edilen tutarlı bir yoğunluk profili kullanılmıştır. Vorteksin komşuluğunda bulunan radyal yoğunluk profili, ses hızının da bir radyal dağılımını gerektirmektedir. Böylece hem olay ufku ile ergo-kürenin konumları hem de tüm yayılım dinamiği bir önceki duruma göre farklılaşmış olmaktadırlar. Tez çalışmasında zaman-aralıklarında ve bundan bağımsız asimptotik frekans-aralıklarında süper-ışıma

bu kez tekrar incelenmiştir. Sonuçta, süper-ışıma dinamiği incelenirken sabit yoğunluk kullanımı ile tutarlı yoğunluk profilinin kullanımı karşılaştırıldığında, tutarlı bir yoğunluk profilinin süper-ışıma genliğinin zamansal değişimini düzenlediği ve spektral değişimini özellikle düşük frekanslarda etkilediği gösterilmiştir.

ACKNOWLEDGMENTS

I would like to express my deepest gratitude to my advisors Prof. Tekin Dereli and Assoc. Prof. Kaan Güven for all the time, advice and energy they gave to make my Ph.D. experience both productive and valuable. It was an incredible opportunity for me to be a Ph.D. student of such great physicists.

I acknowledge Prof. Ayşe Hümeyra Bilge, Prof. Özgür Müstecaplıoğlu, Assoc. Prof. Mehmet Özgür Oktel and Prof. Metin Muradoğlu for being in my thesis committee.

I would like to acknowledge the financial support from the Scientific and Technological Research Council of Turkey (TÜBİTAK)-BIDEB 2211 National Scholarship Program for PhD Students.

I must express my very profound gratitude to my family for providing me with unfailing support and continuous encouragement throughout.

TABLE OF CONTENTS

LIST OF FIGURES

Chapter 1

INTRODUCTION

1.1 Black Holes in General Relativity

The prediction of the existence of black holes(BH) emerges from the solutions of field equations in General Relativity. After a massive object with a minimal mass of $\sim 3M_{\odot}$ ($M_{\odot}$ is the solar mass), has undergone a complete gravitational collapse, it leaves a black hole behind. This forms a region in space where the gravity is so intense that not even light can escape [1]. The term "black hole" was first used by John A. Wheeler in 1967 to describe an object resulting from a gravitational collapse [2]. While the mathematical formulation dates back to 1915 when Albert Einstein introduced the theory of general relativity(GR). The theory passed its first test in 1919 when the bending of star light was observed during a solar eclipse [3]. GR is defined via Einstein's field equations, while the challenge is to find a metric that satisfies them. Karl Schwarzschild in 1916 formulated a gravitational field generated by a static point mass which satisfies the Einsteins equations, known as the Schwarzschild metric which yielded the simplest known BH, one with no electric charge or angular momentum, the most general spherically symmetric vacuum solution of the Einsteins field equations [4]. For a rotating uncharged axially-symmetric BH (Kerr black hole), it took almost 50 years to find a solution. The Kerr metric was discovered in 1963 by Roy Kerr [5]. Black Holes are mainly categorized by their electric charge and angular momentum: Schwarzschild (uncharged, non-rotating) black holes, Kerr (uncharged, rotating) black holes, Reissner-Nordström (charged, non-rotating) black holes and Kerr-Newman (charged, rotating) black holes.

Figure 1.1: The first image of a black hole, using Event Horizon Telescope observations of the center of the galaxy M87. Retrieved from https://eventhorizontelescope.org

Experimentally, last years have been very rewarding for astrophysical researches. The Laser Interferometer Gravitational-Wave Observatory collaboration(LIGO) announced the first direct detection of gravitational waves resulting from a black hole merger in February 2016 [6]. After the first observation, more data from merging black holes and binary neutron merger observations are reported [7]. On April 10, 2019, Event Horizon telescope announced first ever direct image of a black hole at the center of the galaxy M87 (Fig.1.1) [8].

While the observations of BH recently achieved, direct observations of the phenomena theorized for BH such as Hawking radiations and superradiance are still beyond our reach. One of the effects theorized by Roger Penrose in 1969 is called the Penrose process [9]. In order to account for the loss of angular momentum, Penrose argued that any particle that enters a region called ergosphere, i.e region around rotating black holes in which particles can no longer remain stationary in space, could be scattered and ejected with greater energy than the one they initially had . The wave counterpart of the Penrose process is called superradiance, which was first suggested by Zel'dovich in 1971 [10]. Zel'dovich pointed out that a cylinder made of an absorbing material, rotating around its axis can amplify incident waves under certain conditions.

Another famous effect is the Hawking Radiation. Hawking's semiclassical approach to black holes in 1974, by applying the techniques of quantum field theory in curved spacetimes to the formation of a Schwarzschild black hole, showed that black holes should emit particles with a characteristic temperature proportional to the area of the BH [11,12]. The calculated Hawking radiation from a black hole with the size of one solar mass is $\sim 10^{-7}K$, which makes astrophysical observation nearly impossible. The idea of thermal emission is also supported by thermodynamic arguments [13].

1.2 Analog Black Holes

Even though the direct observation of BH has been achieved, observing the predicted effects, Hawking radiation and superradiance, are still an open issue. Analogue models of gravity present alternative ways to detect such phenomena to some extent. The general idea behind is that in many physical systems it is possible to identify suitable excitations that propagate as fields on a curved spacetime (CS). That allows constructing an analogy between the excitations, i.e sounds, traveling in flat Minkowski spacetime but coupled to CS metric, with the light traveling on a CS near BHs. Thus, starting from non-relativistic equations, the excitations are shown to be endowed with a Lorentz invariant dynamics where the Lorentz group is associated with an invariant speed coinciding with the speed of sound. Thus, the analogies wish to avoid the observability problem caused by the fact that, the aforementioned effects are very subtle and the observing in GR systems experimentally very difficult. A number of analogue systems have been proposed in different medias such as condensed-matter, optical systems or superfluids, and the experimental realizations gained popularity in the last decades as explained in the next part. Analog systems are easier to handle compared to gravitational systems as such; instead of solving complicated non-linear dynamical equations for the gravitational fields, in analogue gravity, an effective geometry resulted from the equations of motion of the system, usually the wave propagation. However, the question is how much of general relativity can be analyzed when mapped into analogue systems. One big difference is that the analogy isolates only the kinematic aspects of gravity. The dynamics of the BH are governed by the Einsteins field equations whereas the analogy governed by the fluid equations of motion. In other words, perfect fluids mimic the kinematical aspects of general relativity, i.e, those properties which depend only upon the geometry of spacetime. The black hole configurations and the propagation of fields in curved relativistic spacetimes are the features that can be mapped [14]. Therefore, the interaction between the matter fields and the analogue geometric tensors are outside the analogue properties since there are currently no known analogue systems that reproduce the Einstein equations, which is why the analogy does not extend to the dynamical level.

As an important note, while it is possible to construct analogue Schwarzschild geometries, with an acoustic horizon (explained in section 3.5), acoustic Kerr is highly non-trivial. In fact it has been shown that the simulation of Kerr geometry in fluids, up to a conformal factor, is impossible [15]. However, the ergoregion and the event horizon concepts do not rely on the exact solution of the Kerr geometry. That shows any system possessing two horizons may be used to study Hawking radiation or the superradiance phenomena. In addition, it has been shown that (2+1 dimensional) equatorial plane of the Kerr geometry which posses two horizons can be mapped as an analogy.

1.3 Brief History

While the bases of the idea that the propagation of sound waves in inviscid fluids following a relativistic metrics are known [16], in 1981 Unruh first showed the possibility of studying gravitational phenomena, that are otherwise impossible to study experimentally, via black hole analogies [17]. After a decade later, Jacobson took this analogy as a guide to study the trans-Planckian problem[1]in Hawking radiation [18]. In 1998 Visser rediscovered and gave mathematical proofs for the phenomena associated with black holes to their equivalence with the analogies such as ergoregion, event horizon and surface gravity [14]. In condensed matter systems, 3He by Volovik and Jacobson is the first condensed matter system to be implemented to the analogy [19,20]. The possibility of detecting Hawking radiation gained some popularity not only in condensed matters but in more general analogue spacetimes as well [21–24].

In 2000 the first use of Bose-Einstein condensation(BEC) as an analogue model was proposed for the detection of Hawking radiation [25, 26]. BEC gained popularity among the proposed analog models (explained in section 3.3) [27–29]. The phenomena is also investigated widely for solid state models [30, 31], optical systems [32–35], relativistic fluids [36], superfluid Helium [37, 38] shallow water systems [39–41]. General review on different models is given in [42].

On the other hand, the experimental studies emerged only within the last few years. Experimental realizations of horizons were reported in water channels [43] and atomic BECs [44]. Recently, rotational superradiant scattering in a water vortex flow was reported [45]. An acoustic black hole in a needle-shaped BEC of Rubidium-87 was achieved and recently spontaneous Hawking radiation, stimulated by quantum vacuum fluctuations, emanating from an analogue black hole in an atomic BEC was reported [46, 47].

1.4 Thesis plan

The purpose of this thesis is to study the superradiance phenomena in BEC vortex systems considering different density approaches. The numerical study is useful to investigate the effects of different variables, such as the density, the rotational frequency of a fluid or the event horizon location. Chapter 2 is intended as an introduction to explain how the analogy is first set in classical fluids and includes the derivation of

[1]Near event horizon, the frequency of a quanta must have an infinite value when it is traced back from infinity where it is detected. Infinite frequency thus the wavelength becomes shorter than the Planck length referred as the trans-Plankian problem.

the metric and the equation of motion for the fluctuations traveling in the medium.

Chapter 3 includes a brief definition of the BEC and the formulation of the BH analogy in BEC with the hydrodynamic description of the condensate (Sec.3.2.1) and the appropriate approximation that is used to form the effective metric (Sec.3.2.3). In Section 3.4, we set up a vortex structure which is necessary to calculate the event horizon and the ergoregion for the draining-bathtub model(DBT) implemented in two different density profiles (Sec. 3.5).

Chapter 4 explains the superradiance phenomena and a few of the experimental studies conducted in the last few years.

Finally, in chapter 5, we showed the methodology used to analyze the Klein Gordon equation numerically (Sec.5.1) and the numerical results which show the superradiance effect for the constant density approximation (Sec.5.2) and the self-consistent density profile (Sec.5.3) both in the time and the frequency domains.

In chapter 6, we briefly discussed the results of the analysis.

Appendix A gives the null vector calculations of the effective metric for the propagation field.

Appendix B gives the detailed formulation of the wave equation in the frequency domain.

Appendix C shows the explicit derivation of conjugate fields.

Chapter 2

BLACK HOLE ANALOGY IN CLASSICAL FLUIDS

Gravitational analogy started with Unruh in 1981, when he realized the equivalency between the waves traveling through a fluid under certain assumptions with the field propagating in a curved spacetime [17]. He derived the formulation by a fluid that is inviscid, barotropic and has an irrotational flow, and showed the resulted equation is, in fact, a massless Klein-Gordon equation for sound waves rather than light [48],

$$\frac{1}{\sqrt{-g}} \sum_{i,j} \frac{\partial}{\partial x^i} \left(\sqrt{-g} g^{ij} \frac{\partial}{\partial x^j} \Phi \right) = 0. \tag{2.1}$$

Here Φ is a scalar field, in our analogy Φ represents the small perturbations in velocity potential, g_{ij} is the acoustic metric depending on the density and the velocity of the background, i.e fluid. The mathematical equivalence, shown in detail in section 2.1, is the idea behind any analogue black hole systems, although, for different medias derivations may slightly change such as in the case of Bose-Einstein condensates derived in section 3.2.

2.1 Derivation of the Acoustic Metric

There are two main equations describing the fluid dynamics: the continuity equation

$$\frac{\partial \rho}{\partial t} + \nabla \cdot (\rho \vec{v}) = 0, \tag{2.2}$$

and the Euler equation

$$\rho\frac{d\upsilon}{dt} \equiv \rho\left[\partial_t\vec{\upsilon} + (\vec{\upsilon}\cdot\nabla)\vec{\upsilon}\right] = \vec{F}. \tag{2.3}$$

Here υ is the velocity of the fluid, ρ is the density field and $\vec{F}$ shows the net external force defined in Euler equation as

$$\vec{F} = -\nabla p - \rho\nabla U_e - \rho\nabla U_g, \tag{2.4}$$

where U_e is the potential of the external driving force, U_g is the gravitational potential and p is the pressure term. Substituting the identity $\frac{1}{2}\nabla\left(\vec{\upsilon}\cdot\vec{\upsilon}\right) = \vec{\upsilon}\times(\nabla\times\vec{\upsilon}) + (\vec{\upsilon}\cdot\nabla)\vec{\upsilon}$ with the defined external force, $\vec{F}$, to the Euler equation (2.3) yields

$$\partial_t\vec{\upsilon} = \frac{-\nabla p}{\rho} - \nabla U_e - \nabla U_g - \frac{\nabla\upsilon^2}{2} + \vec{\upsilon}\times(\nabla\times\vec{\upsilon}). \tag{2.5}$$

Furthermore, the fluid is assumed to be barotropic, i.e the density is a function of the pressure only, $p = p\left(\rho\right)$, with that we can define the enthalpy from the first law of thermodynamics

$$dH = TdS + Vdp \tag{2.6}$$

and with the barotropic assumption, specific enthalpy can be written as

$$h\left(p\right) = \int_0^p \frac{dp'}{\rho\left(p'\right)} \quad \Rightarrow \nabla h = \frac{\nabla p}{\rho}. \tag{2.7}$$

The next assumption is the locally irrotational flow, in other words, the vorticity free fluid, where the velocity is defined in terms of a velocity potential Φ

$$\vec{\upsilon} = -\nabla\Phi. \tag{2.8}$$

Inserting the enthalpy, and the velocity potential to the Eq. 2.5 gives

$$-\partial_t \nabla\Phi - \nabla\Phi \times (\nabla \times \nabla\Phi) + \nabla h + \nabla(\frac{(\nabla\Phi)^2}{2} + U_e + U_g) = 0, \tag{2.9}$$

and integrating this over a closed surface gives a Bernoulli type of equation

$$-\partial_t \Phi + h + (\frac{(\nabla\Phi)^2}{2} + U_e + U_g) = 0. \tag{2.10}$$

Next, we introduce small (first order in ϵ) perturbations in the background ρ_0, p_0, Φ_0 and in the velocity of the fluid υ_0 and discard the higher order terms;

$$\rho = \rho_0 + \varepsilon\rho_1, \qquad p = p_o + \varepsilon p_1, \qquad \Phi = \Phi_0 + \varepsilon\Phi_1, \qquad \upsilon = \upsilon_0 + \varepsilon\upsilon_1. \tag{2.11}$$

Starting with the enthalpy equation (2.7), by Taylor expansion we can write

$$h = h_0 + \frac{\partial h}{\partial p}(p - p_0) = h_0 + \frac{1}{r_0}(p - p_0), \tag{2.12}$$

$$h = h_0 + \varepsilon\frac{p_1}{\rho_0}. \tag{2.13}$$

The Euler equation (2.9) with the perturbations becomes

$$-\partial_t(\Phi_0 + \varepsilon\Phi_1) + h_0 + \varepsilon\frac{p_1}{\rho_0} + (\frac{(\nabla\Phi_0 + \varepsilon\Phi_1)^2}{2} + U_e + U_g) = 0. \tag{2.14}$$

The zeroth order and the first order equations in ε yield the unperturbed Euler equation for the background

$$-\partial_t\Phi_0 + h_0 + (\frac{(\nabla\Phi_0)^2}{2} + U_e + U_g) = 0, \tag{2.15}$$

and an equation for the phase perturbations

$$-\partial_t\Phi_1 + \frac{p_1}{\rho_0} + \nabla\Phi_1 \cdot \nabla\Phi_0 = -\partial_t\Phi_1 + \frac{p_1}{\rho_0} - \nabla\Phi_1 \cdot \vec{\upsilon}_0 = 0, \tag{2.16}$$

which gives the pressure perturbation as

$$p_1 = \rho_0(\nabla\Phi_1 \cdot \vec{v}_0 + \partial_t\Phi_1). \tag{2.17}$$

Second, we apply the Taylor expansion to the density function around the pressure p_0 as the barotropic condition allows us to do

$$\rho\,(p) = \rho(p_0) + \frac{d\rho}{dp}(p - p_0) \quad \Rightarrow \rho_1 = \frac{\partial\rho}{\partial p}p_1 \tag{2.18}$$

with the definition of p_1 in the Eq.2.17

$$\rho_1 = \frac{\partial\rho}{\partial p}\rho_0(\nabla\Phi_1 \cdot \vec{v}_0 + \partial_t\Phi_1). \tag{2.19}$$

We can know insert all to the continuity equation (2.2)

$$\frac{\partial(\rho_0 + \varepsilon\rho_1)}{\partial t} + \nabla \cdot ((\rho_0 + \varepsilon\rho_1)(\vec{v}_o + \varepsilon\vec{v}_1)) = 0 \tag{2.20}$$

and again discard the terms with ϵ^2 and higher. Resulted equations are the continuity equation for the background density

$$\frac{\partial\rho_0}{\partial t} + \nabla \cdot (\rho_0\vec{v}_0) = 0, \tag{2.21}$$

and an equation for the density perturbation

$$\frac{\partial\rho_1}{\partial t} + \nabla \cdot (\rho_1\vec{v}_0 + \rho_0\vec{v}_1) = 0. \tag{2.22}$$

Substituting Eq.2.19 into Eq.2.22 gives

$$\partial_t\left(\frac{\partial\rho}{\partial p}\rho_0(\nabla\Phi_1 \cdot \vec{v}_0 + \partial_t\Phi_1)\right) + \nabla \cdot \left(\frac{\partial\rho}{\partial p}\rho_0(\nabla\Phi_1 \cdot \vec{v}_0 + \partial_t\Phi_1)\vec{v}_0 + \rho_0\vec{v}_1\right) = 0, \tag{2.23}$$

and with the speed of sound $\frac{1}{c} = \sqrt{\frac{d\rho}{dp}}$ and the velocity perturbation $\upsilon_1 = -\nabla\Phi_1$ final equation becomes

$$-\frac{\rho_0}{c^2}\partial_t\left(\nabla\Phi_1 \cdot \vec{\upsilon}_0 + \partial_t\Phi_1\right) + \frac{\rho_0}{c^2}\nabla\cdot\left(c^2\nabla\Phi_1 - \left(\nabla\Phi_1\cdot\vec{\upsilon}_0 + \partial_t\Phi_1\right)\vec{\upsilon}_0\right) = 0. \qquad (2.24)$$

One can write the final equation in the form of the Klein-Gordon equation for a massless scalar field

$$\frac{1}{\sqrt{-g}}\partial_\mu\left(\sqrt{-g}g^{\mu\nu}\partial_\nu\Phi_1\right) = 0, \qquad (2.25)$$

where g is the determinant of the inverse metric $g^{\mu\nu}$; $g = \det(g_{\mu\nu})$. Which gives the acoustic metric and its invert as,

$$g^{\mu\upsilon} \equiv \frac{1}{c\rho_0}\begin{pmatrix} -1 & -\upsilon_0^j \\ -\upsilon_0^i & (c^2\delta^{ij} - \upsilon_0^i\upsilon_0^j) \end{pmatrix} \Leftrightarrow g_{\mu\nu} \equiv \frac{\rho_0}{c}\begin{pmatrix} -(c^2 - \upsilon_0^2) & -\upsilon_0^j \\ -\upsilon_0^i & \delta_{ij} \end{pmatrix} \qquad (2.26)$$

with the determinant of the metric

$$-g = \frac{\rho_0}{c^2} > 0, \qquad (2.27)$$

and the line element

$$ds^2 = g_{\mu\nu}dx^\mu dx^\nu = \frac{\rho_0}{c}\left[-c^2dt^2 + (dx^i - \upsilon_0^i dt)\delta_{ij}(dx^j - \upsilon_0^j dt)\right], \qquad (2.28)$$

where $x^{\mu,\nu} \equiv (t, x^i)$ and μ, ν run from 0 to 3 while i, j run from 1 to 3.

2.1.1 Assumptions regarding the derivation

Here we have two metrics, one is the physical spacetime metric that the fluid couples, which is the usual flat Minkowski background, (3+1) real vector space with signature $(-, +, +, +)$, and the other one is acoustic metric $g_{\mu\nu}$, that the perturbation couples which is a curved (3+1)-dimensional Lorentzian spacetime geometry [49].

In addition, three assumptions made to derive the analogy play a critical role; irrotational, inviscid fluid flow and barotropic condition. In order to define a velocity potential which forms the analog scalar field in the final equation, irrotationality is the key. And since any failure in the barotropic condition which in turn fails the irrotationality, two assumptions are dire to the derivation of the metric [42]. While the viscosity is also important in our derivation, there are scenarios where the viscous fluids still allow an analogy to form [40].

Another assumption made in the derivation is the first order fluctuations. Any non-linearity of the hydrodynamical equations will affect the fluid flow making the derivation moot [50]. Also, the density and the velocity are assumed to be continuous fields as such the microscopic structure of the fluid can be ignored. Since, at high frequencies or short wavelengths fluid equation of motion is not applicable, in addition, sound waves can not exist at wavelengths shorter than the inter-atomic spacing.

Finally it is important to note that the metric derivation comes from the continuity equation and the Euler equation compared to the black hole metric which is derived from the Einstein's field equations. Therefore the background behavior is not explained by the analogy, only a wave propagation on a fluid background can be mapped to a wave propagating on a curved space time.

2.2 Discussion

The idea introduced above is for a Newtonian fluid under certain assumptions. While the analogy holds to observe the aforementioned effects, superradiance and Hawking radiation, there are obstacles to overcome. Experiments performed at the University of Nottingham, the Quantum Gravity Laboratory, created a region in water flows in which the wave traveling upstream will encounter an obstacle they can not cross, i.e the effective horizon. With this set-up, the group reported the presence of negative mode conversion, a basic ingredient of the Hawking effect [41, 51, 52]. In addition, the observation of Bogoliubov coefficients is reported [43], which was considered as the thermal properties of stimulated Hawking radiation. However, the results of the mode conversion or the Hawking radiation is under discussion due to the produced regions in both experiments were not supercritical in the group velocity for all the relevant frequencies. Although the scattered waves acquire negative norm components, i.e presence of negative mode conversion, part of this conversion appears to come from scattering between two different subsonic (subcritical) regimes. Therefore, whether the effect is due to the horizon or not is under debate [53, 54].

The important difference here is that the Hawking radiation is spontaneous thermal radiation, and considering the effect is very subtle, water flow experiments are unable to detect the analogue of spontaneous Hawking radiation due to the overwhelming thermal effects of the setup itself.

Another effect mentioned is the superradiance, energy extraction at the expense of rotational energy by a scattering wave. Compared to the Hawking effect, observing superradiance is considered to be much simpler, since there are no temperature restrictions and the fact that the parameters affecting the energy gain such as rotational frequency of the fluid can be controlled and increased to a point. The experiments considering classical fluids by the Quantum Gravity laboratory [45, 55] reported amplification of the incident wave. There are many other theoretical and experimental works using different systems sucs as; optical systems, superfluids and Bose-Einstein condensates, a detailed explanation is given in section 4.

Chapter 3

BOSE-EINSTEIN CONDENSATES

The gravitational model with BEC is one of the most studied analog systems of gravity. As mentioned in Sec.1.3, it is the first quantum system to be successfully proposed [26] and extensively investigated for different flow configurations corresponding to different geometries [27, 56, 57]. Especially for the Hawking radiation, numerical, analytical as well as experimental investigations have been a big part of the analog gravity models [58–63]. In 2010, event horizon was created in a system consisting of 87Rb atoms by using a harmonic trap and a step-like potential, showing that the condensate could be accelerated to a velocity higher than the speed of sound propagating in BEC [44]. After that, black-hole laser configuration, showing the existence of phononic excitations was reported [46], although the observation of spontaneous self-amplifying Hawking radiation has been challenged [64,65]. In 2016 Hawking particles produced by a single black-hole horizon was again reported, this time by using the correlation function between the outgoing and the ingoing Hawking pairs [47]. While there are some discussions about the origin of the radiation signal [66–68], there is also positive feedback to the result of the experiment [69]. Besides Hawking radiation other phenomena such as cosmological particle production in BECs [28, 70, 71], quantum gravity phenomenology [72–74] and superradiance phenomena, that will be the focus of this thesis, have been studied [75].

In this chapter, we present the basics of the theoretical description of BECs (Sec.3.1) and show how the gravitational analogy is set (Sec.3.2). The advantages of BEC over other analog models are explained in section 3.3. Finally, the vortex models for a constant density and a non-constant background density profiled are derived (Sec.3.4) which provides a description of the analog event horizon and the ergoregion for our system (Sec.3.5).

3.1 Theory of BEC

BEC is a gas of indistinguishable bosons in which the atoms are confined in traps and cooled down to low enough temperatures (in the order of μK). The macroscopic amount of the condensate led to occupy a single quantum state, the ground state of the system determined by a trap. The theoretical prediction of the BEC dates back to 1924 by Satyendra Nath Bose [76] and Albert Einstein [77], where the idea was explained as N bosonic particles in a cubic box would undergo a phase transition at a specific temperature as such

$$T_c = 3.31\frac{\hbar^2\rho^{2/3}}{mk_B} \tag{3.1}$$

where m is the mass of the bosons, ρ is the particle density and k_B is the Boltzmann constant. The number of particles in the ground state (N_0) is considerably larger for temperatures $T < T_c$,

$$\frac{N_0}{N} \rightarrow 0, T > T_c, \qquad \frac{N_0}{N} \rightarrow 1 - \left(\frac{T}{T_c}\right)^{3/2}, T < T_c. \tag{3.2}$$

At high temperatures gas is described by classical physics, given example is "the billiard balls", while the temperature gets lowered but still higher than the critical temperature defined, particles are still classical but the collisions are treated by quantum mechanics. When the temperature reaches a critical value there is a matter wave overlap and finally below T_c, a giant matter wave due to constructive interference of all the waves describing particles in the lowest quantum level accessible, creates a BEC [78].

Bose Einstein condensation was first experimentally observed in 1995 at JILA in rubidium (87Rb) [79], and at MIT in sodium (23Na) [80] after the advances of laser cooling and magnetic trapping made it possible to cool down the condensate in the order of μK. Later the occurrence of BEC in vapors of lithium (7Li) [81] was also reported. Although the experiments started in 1995, the theoretical aspects are much older and grew in interdisciplinary areas.

3.2 Analog Black Holes in Bose Einstein Condensates

In a quantum system of N interacting bosons in which the most of the bosons lie in the same single particle quantum state, the system can be described by the Hamiltonian of the form;

$$H = \int dx \hat{\Psi}^{\dagger}(t,x)\left[-\frac{\hbar^2}{2m}\nabla^2 + V_{ext}(x)\right]\hat{\Psi}(t,x) \tag{3.3}$$

$$+\frac{1}{2}\int dx dx' \hat{\Psi}^{\dagger}(t,x)\hat{\Psi}^{\dagger}(t,x')V(x-x')\hat{\Psi}^{\dagger}(t,x')\hat{\Psi}^{\dagger}(t,x). \tag{3.4}$$

Here $-\frac{\hbar^2}{2m}\nabla^2$ term represents the kinetic energy operator, V_{ext} is the external potential or the trap potential and $V(x-x')$ is the interatomic two-body potential, m is the mass of the bosons and $\hat{\Psi}^{\dagger}(t,x)$ is the boson field operator which is defined as classical contribution $\psi(t,x)$ plus excitations $\hat{\varphi}$. In the non relativistic limit when the most of the atoms lie on the ground state, the interatomic interaction is defined as $V(r-r') = U_0\delta(r-r_0)$ with

$$U_0 = \frac{4a\pi\hbar^2}{m} \tag{3.5}$$

which is a coupling constant characterized by a single parameter a, defined as a scattering length for binary interactions between atoms and must be positive to prevent an instability leading to a collapse.

Omitting the quantum fluctuations $\hat{\varphi}$, we can write the equation for a weakly interacting boson condensate known as the Gross-Pitaevskii equation (GP)

$$i\hbar\frac{\partial\psi}{\partial t} = \left(-\frac{\hbar^2}{2m}\nabla^2 + V_{ext} + U_0\left|\psi\right|^2\right)\psi(r,t), \tag{3.6}$$

which involves both the kinetic energy term, and the repulsive Hartree potential

$V_H = U_0 \left|\psi\right|^2$. Density of the condensate is given as

$$\rho(r,t) = \left|\psi(r,t)\right|^2 . \tag{3.7}$$

The stationary solution can be written as $\psi(r,t) = \psi(r)e^{-i\mu t/\hbar}$, where μ is the chemical potential derived from the interparticle energy of the condensate $E_0 \approx \frac{1}{2}\frac{U_0 N^2}{V}$ with N is the number of particles and V is the volume of the system

$$\mu = \left(\frac{\partial E_0}{\partial N}\right)_V = U_0\rho = \frac{4a\pi\hbar^2\rho}{m}. \tag{3.8}$$

The pressure is derived from the thermodynamic relation

$$p = \left(\frac{\partial E_0}{\partial V}\right)_N = \frac{E_0}{V} = \frac{1}{2}U_0\rho^2 \tag{3.9}$$

and the corresponding bulk speed of sound c is

$$c^2 = \frac{1}{m}\left(\frac{\partial p}{\partial \rho}\right) = \frac{U_0\rho}{m} = \frac{4a\pi\hbar^2\rho}{m^2}. \tag{3.10}$$

On dimensional grounds, the balance between the kinetic energy term and the repulsive Hartree potential implies a correlation or healing length

$$\xi^2 = \frac{\hbar^2}{2\rho m U_0} = \frac{1}{8\pi\rho a}. \tag{3.11}$$

It is described as the distance which the wave function of the condensate tends to its bulk value when subjected to localized perturbations [82], [83].

3.2.1 Hydrodynamic description of BEC

The GP equation (3.6) is recast in a hydrodynamic form by writing the condensate wave function in terms of its magnitude, $|\psi(r,t)|$, and phase, $\Phi(r,t)$, which is called the Madelung representation or the WKB approximation

$$\psi = |\psi(r,t)|\, e^{i\Phi(r,t)} = \sqrt{\rho\,(r,t)}e^{i\Phi(r,t)}. \tag{3.12}$$

And the particle current density is

$$j = -\frac{i\hbar}{2m}\left(\psi^*\nabla\psi - \psi\nabla\psi^*\right) = \rho(r,t)\frac{\hbar\nabla\Phi}{m}, \tag{3.13}$$

where the hydrodynamic relation $j = \rho v$ gives the background fluid velocity as

$$\vec{v} = (\hbar/m)\nabla\Phi. \tag{3.14}$$

Now we can insert the wave function 3.12 into the GP equation 3.6;

$$i\hbar\frac{\partial\left(\sqrt{\rho}e^{i\Phi}\right)}{\partial t} = \left(-\frac{\hbar^2}{2m}\nabla^2 + V_{ext} + U_0\rho\right)\sqrt{\rho}e^{i\Phi}, \tag{3.15}$$

$$\begin{aligned} i\hbar\left(\frac{e^{i\Phi}}{2\sqrt{\rho}}\frac{\partial\rho}{\partial t} + i\sqrt{\rho}e^{i\Phi}\frac{\partial\Phi}{\partial t}\right) =& -\frac{\hbar^2}{2m}\nabla\cdot\left(\frac{e^{i\Phi}}{2\sqrt{\rho}}\nabla\rho + i\sqrt{\rho}\nabla\Phi e^{i\Phi}\right) \\ &+ \left(V_{ext} + U_0\rho\right)\sqrt{\rho}e^{i\Phi}, \end{aligned} \tag{3.16}$$

$$\begin{aligned} i\hbar\left(\frac{1}{2\sqrt{\rho}}\frac{\partial\rho}{\partial t} + i\sqrt{\rho}\frac{\partial\Phi}{\partial t}\right) =& -\frac{\hbar^2}{2m}\left(\frac{\nabla^2\rho}{2\sqrt{\rho}} + \frac{i\nabla\rho\nabla\Phi}{\sqrt{\rho}} - \frac{|\nabla\rho|^2}{4\rho^{3/2}} + i\sqrt{\rho}\nabla^2\Phi - \sqrt{\rho}\,|\nabla\Phi|^2\right) \\ &+ \left(V_{ext} + U_0\rho\right)\sqrt{\rho}. \end{aligned} \tag{3.17}$$

The final form generates two equations; one from the complex part

$$\frac{\partial\rho}{\partial t} = -\frac{\hbar}{m}\nabla\rho\nabla\Phi - \frac{\hbar}{m}\rho\nabla^2\Phi \tag{3.18}$$

with the velocity defined in Eq.3.14 which gives the continuity equation,

$$\frac{\partial \rho}{\partial t} + \vec{\nabla} \cdot (\rho \vec{v}) = 0, \tag{3.19}$$

. and one from the real part

$$-\hbar \frac{\partial \Phi}{\partial t} = -\frac{\hbar^2}{2m} \left(\frac{\nabla^2 \rho}{2\rho} - \frac{|\nabla \rho|^2}{4\rho^2} - |\nabla \Phi|^2 \right) + (V_{ext} + U_0 \rho), \tag{3.20}$$

with the velocity defined

$$\partial_t \vec{v} + (\vec{v} \cdot \vec{\nabla}) \vec{v} = \frac{\hbar^2}{2m^2} \vec{\nabla} \left(\frac{1}{\sqrt{\rho}} \vec{\nabla}^2 \sqrt{\rho} \right) - \frac{\vec{\nabla} V_{ext}}{m} - \frac{\vec{\nabla}(U_0 \rho)}{m} \tag{3.21}$$

gives the Euler equation with an extra term containing $\hbar^2$, called the quantum pressure term. Here, due to the nature of the velocity (3.14) the term $\vec{v} \times (\nabla \times \vec{v})$ is zero.

3.2.2 First order fluctuations and the effective metric

Phonons, i.e acoustic waves are the linear perturbations of the background solutions, Eq.s 3.19 and 3.21. In order to investigate the propagation of the fluctuations in the condensate, we linearize the equations around the background $\rho = \rho_0 + \epsilon \rho_1$, $\Phi = \Phi_0 + \epsilon \Phi_1$, and the velocity $\upsilon = \upsilon_0 + \epsilon \upsilon_1$;

$$\frac{\partial (\rho_0 + \epsilon \rho_1)}{\partial t} + \vec{\nabla} \cdot ((\rho_0 + \epsilon \rho_1) \vec{v}_0 + \epsilon \vec{v}_1) = 0 \tag{3.22}$$

which in turns gives two equation, the continuity equation for the background density

$$\frac{\partial \rho_0}{\partial t} + \nabla \cdot (\rho_0 \vec{v}) = 0, \tag{3.23}$$

and one for the density fluctuations

$$\frac{\partial \rho_1}{\partial t} + \nabla \cdot (\rho_0 \upsilon_1) + \nabla \cdot (\rho_1 \upsilon_0) = 0. \tag{3.24}$$

Second, we apply the linearization to the Eq.3.20

$$-\hbar\frac{\partial\left(\Phi_0+\epsilon\Phi_1\right)}{\partial t}=-\frac{\hbar^2}{2m}\left(\frac{\nabla^2\left(\rho_0+\epsilon\rho_1\right)}{2\left(\rho_0+\epsilon\rho_1\right)}-\frac{\left|\nabla\left(\rho_0+\epsilon\rho_1\right)\right|^2}{4\left(\rho_0+\epsilon\rho_1\right)^2}-\left|\nabla\left(\Phi_0+\epsilon\Phi_1\right)\right|^2\right)$$
$$+V_{ext}+U_0\left(\rho_0+\epsilon\rho_1\right), \tag{3.25}$$

$$-\hbar\frac{\partial\left(\Phi_0+\epsilon\Phi_1\right)}{\partial t}=-\frac{\hbar^2}{2m}\left(\frac{\nabla^2\rho_0+\epsilon\nabla^2\rho_1}{2\rho_0}\left(1-\epsilon\frac{\rho_1}{\rho_0}\right)-\frac{\left|\nabla\left(\rho_0+\epsilon\rho_1\right)\right|^2}{4\rho_0^2}\left(1-2\epsilon\frac{\rho_1}{\rho_0}\right)\right)$$
$$-\frac{\hbar^2}{2m}\left(\left|\nabla\left(\Phi_0+\epsilon\Phi_1\right)\right|^2\right)+V_{ext}+U_0\left(\rho_0+\epsilon\rho_1\right), \tag{3.26}$$

which in turns gives the Euler equation for the background,

$$-\hbar\frac{\partial\Phi_0}{\partial t}=-\frac{\hbar^2}{2m}\left(\frac{\nabla^2\rho_0}{2\rho_0}-\frac{\left|\nabla\rho_0\right|^2}{4\rho_0^2}-\left|\nabla\Phi_0\right|^2\right)+\left(V_{ext}+U_0\rho_0\right) \tag{3.27}$$

and for the first order fluctuations

$$\frac{\partial\Phi_1}{\partial t}=-\upsilon_0\cdot\nabla\Phi_1-U_0\rho_1+\frac{\hbar^2}{2m}D_2\rho_1, \tag{3.28}$$

where $D_2\rho_1$ is

$$D_2\rho_1=\frac{1}{2\sqrt{\rho_0}}\nabla^2\frac{\rho_1}{\sqrt{\rho_0}}-\frac{\rho_1}{2\rho_0^{3/2}}\nabla^2\sqrt{\rho_0}. \tag{3.29}$$

Eq.s 3.27-3.20 and Eq.s 3.19-3.23 show that the total wave equations $\left(\sqrt{\rho}e^{i\Phi}\right)$ and the background wave equations $\left(\sqrt{\rho_0}e^{i\Phi_0}\right)$ satisfy the GP equation separately.

3.2.3 Hydrodynamic(Quasiclassical) approximation

In order to use BEC models as an analogy for the gravitational systems, we hope to reach the Klein Gordon equation that will show us the mathematical equality between the propagation of the linearized phase Φ_1 and the propagation of light in a curved spacetime. Here D_2 is a messy second-order differential operator and there are several approximations mentioned in [84] mainly to deal with this quantum pressure term. However, there are no numerical or analytical works that calculate the quantum pressure effects in the superradiance studies. At this point, we face a conundrum: The so-called hydrodynamic approximation neglects the quantum pressure term, thereby enabling the construction of an effective acoustic metric and the usual quadratic dispersion relation for the wave propagation. One way to justify the approximation, $D_2 = 0$, is to point out that D_2 is always multiplied by $\hbar^2$ and in this sense is suitably small. In the equation above Eq.3.28, the pressure term $U_0\rho_1$ is of the order $U_0\rho/R$ while the quantum pressure term $\frac{\hbar^2}{2m}D_2\rho_1$ is of the order $\hbar^2/mR^3$, where R is the spatial scale [83]. This implies that for

$$R >> \frac{\hbar}{\sqrt{2mU_0\rho}} \equiv \xi \tag{3.30}$$

the quantum pressure term is negligibly small. Unfortunately, the conditions enabling the hydrodynamic approximation may not be satisfied near the event horizon and the curved space-time picture breaks down near the vortex, revealing the underlying quantum structure. Hence, in a BEC, the full (nonlinear) scattering from a vortex appears to be incompatible with a classical relativistic treatment.

However, for linearized fluctuations, a "forced" hydrodynamic approximation can still capture the essence of the dynamics, provided that the quantum potential remains small compared to Hartree potential, $U_0\rho_1$. This is the standard practice for the low frequency fluctuations against a constant background density [85], [86].

In the case of radially changing density, we have to elaborate a bit more. We note that when the background density $\rho_0(r)$ is radially smooth function, the low frequency fluctuations are comparably small even near the event horizon. Beyond the horizon, at the deep core of the vortex, this is not true. However, in the numerical computation of the propagation of fluctuations (section 5.1.1), we describe a numerical technique that monitors the outgoing waves from the horizon and ensures that they do not contribute to the scattered waves in the physical domain. The ratio of the Hartree potential and the leading term of the quantum potential can be written as

$$\frac{\frac{\hbar^2}{2m}D_2\rho_1}{U_0\rho_1} = \frac{\nabla\cdot\left(\rho_0\nabla\left(\frac{\rho_1}{\rho_0}\right)\right)}{2\rho_1}, \tag{3.31}$$

thus we demand that

$$\rho_1''/2\rho_1 < 1. \tag{3.32}$$

The ratio ρ_1''/ρ_1 calculated by the "forced" hydrodynamic approximation shows that this condition is satisfied near the event horizon. With $\frac{\hbar^2}{2m}D_2\rho_1 = 0$,

$$\rho_1 = -\frac{1}{U_0}\frac{\partial\Phi_1}{\partial t} - \frac{1}{U_0}\upsilon_0\cdot\nabla\Phi_1 \tag{3.33}$$

and after we insert ρ_1 to the Eq.3.24, with $\upsilon_1 = \frac{\hbar}{m}\nabla\Phi_1$ and $c^2 = \frac{U_0\rho}{m}$ from the definition Eq.3.10, the final form becomes

$$\frac{\partial}{\partial t}\left[\frac{\rho_0}{c^2}\left(\frac{\partial\Phi_1}{\partial t} + \vec{\upsilon}_0\cdot\nabla\Phi_1\right]\right) - \nabla\cdot(\rho_0\nabla\Phi_1) + \nabla\cdot\left[\frac{\rho_0}{c^2}\left(\frac{\partial\Phi_1}{\partial t} + \vec{\upsilon}_0\cdot\nabla\Phi_1\right)\upsilon_0\right] = 0. \tag{3.34}$$

The equation above is similar to the equation derived for a classical fluid (Eq.2.24) and since the approximation used is to omit the quantum pressure term it is expected. The result can be written in four-dimensional notation as

$$\partial_\mu\left(f^{\mu\nu}\partial_\nu\Phi_1\right) = 0, \tag{3.35}$$

$$f^{\mu\nu}(t,r) \equiv \frac{\rho_0}{c^2}\begin{pmatrix} -1 & -\upsilon_0^j \\ -\upsilon_0^i & (c^2h^{ij} - \upsilon_0^i\upsilon_0^j) \end{pmatrix} \tag{3.36}$$

where h^{ij} is a proper dimensionless 3-metric. In any Lorentzian manifold the curved space scalar d'Alembertian is given in terms of;

$$\frac{1}{\sqrt{-g}}\partial_\mu\left(\sqrt{-g}g^{\mu\nu}\partial_\nu\Phi_1\right)=0, \tag{3.37}$$

so that $g=\det(g_{\mu\nu})$ and $\sqrt{-g}g^{\mu\nu}=f_{\mu\nu}$ with $g_{\mu\nu}$ and its inverse $g^{\mu\nu}$ given as

$$g^{\mu\nu}\equiv\frac{\rho_0}{c}\begin{pmatrix}-1 & -\upsilon_0^j\\ -\upsilon_0^i & (c^2h^{ij}-\upsilon_0^i\upsilon_0^j)\end{pmatrix}, g_{\mu\nu}\equiv\frac{\rho_0}{c}\begin{pmatrix}-\left(c^2-\upsilon^2\right) & -\upsilon_0^k h_{kj}\\ -\upsilon_0^i h_{ki} & h_{ij}\end{pmatrix} \tag{3.38}$$

The system analyzed in the next chapters, the fluid vortex, is studied in cylindrical polar coordinates since it is more convenient to define appropriate velocities. The metric in explicit form in cylindrical-polar coordinates can be written as

$$g_{\mu\nu}\equiv\frac{\rho_0}{c}\begin{pmatrix}-\left(c^2-\upsilon^2\right) & -\upsilon_r & -r\upsilon_\theta & -\upsilon_z\\ -\upsilon_r & 1 & 0 & 0\\ -r\upsilon_\theta & 0 & r^2 & 0\\ -\upsilon_z & 0 & 0 & 1\end{pmatrix}, \tag{3.39}$$

$$g^{\mu\nu}\equiv\frac{1}{c\rho_0}\begin{pmatrix}-1 & -\upsilon_r & -\frac{\upsilon_\theta}{r} & -\upsilon_z\\ -\upsilon_r & -c^2-\upsilon_r^2 & -\frac{\upsilon_r\upsilon_\theta}{r} & -\upsilon_r\upsilon_z\\ -\frac{\upsilon_\theta}{r} & -\frac{\upsilon_r\upsilon_\theta}{r} & \frac{c^2-\upsilon_\theta^2}{r^2} & -\upsilon_r\upsilon_z\\ -\upsilon_z & -\upsilon_r\upsilon_z & -\upsilon_r\upsilon_z & c^2-\upsilon_z^2\end{pmatrix}. \tag{3.40}$$

The line element for the analogy is written in the form

$$ds^2=g_{\mu\nu}dx^\mu dx^\nu=\frac{\rho_0}{c}\left[-c^2dt^2+(dx^i-\upsilon_0^idt)\delta_{ij}(dx^j-\upsilon_0^jdt)\right], \tag{3.41}$$

where $x^{\mu,\nu}\equiv(t,x^i)$ and μ,ν run from 0 to 3 while i,j run from 1 to 3.

A few remarks about the importance of the metric and its signature are given in section 2.1. Note that, we derived the acoustic metric from the GrossPitaevskii equation and in classical fluids the same result is also obtained directly by combining and manipulating the Euler and the continuity equations for an irrotational flow of any inviscid and barotropic fluid. We now showed that the wave equation for the propagation of the fluctuation field Φ_1 of the velocity potential (the sound wave), is given by d'Alembertian equation of movement, which is formally identical to the wave equation of a massless scalar field propagating in a curved spacetime.

3.3 Advantages of Bose Einstein Condensates in Black Hole Analogy

As shown in the previous chapter, the analogy is set for any fluid that is barotropic, inviscid and has an irrotational flow. However, there are obvious setbacks to such systems from an experimental point of view.

The first issue is the temperature restrictions. While it may be relatively easy to create an apparent horizon between subsonic and supersonic flows, analog Hawking radiation requires low temperatures. The effect is very subtle, in the order of μK, which becomes indistinguishable from the background noise. Obviously classical fluids lose the necessary conditions at low temperatures, therefore superfluids and BEC become strong alternatives.

The speed of sound is an another factor that separates the classical fluids from the superfluids and BEC systems. Especially to create the horizon and to be able to observe the superradiant effect, much lower speeds are necessary [87].

The superfluid Helium is an another good candidate with an extremely low temperature. Compared to the BEC, the density is several orders of magnitude larger, leading density variations, inter-atomic separation, and the scattering length to be in the same order, and the effects of inhomogeneity take place on a microscopic scale. In addition, two body interactions for superfluid Helium is much more complicated and important, considering the superfluidity arise from fermion pairs behaving as bosons. Therefore the depletion, the number of atoms in the ground state, is in the order of %90, which is problematic when describing the system as a background for black hole analogy.

In the BEC case, the interatomic relation, the pair interaction, is described by a single parameter, making it a much simpler model to analyze theoretically. And from an experimental point of view, manipulating the system is much easier due to low densities and higher depletion rates.

3.4 Vortex structure in BEC

The experimental detection of a vortex in a BEC was reported in 1999 [88]. Afterward, vortex creation using different methods were also reported such as putting the superfluid in rotation through a mechanical stirring [89–91], imprinting a phase pattern on the wave function [92,93], which leads to the formation of a single-vortex state or merging different independent BECs [94], each with a well defined uniform phase and so-called Kibble-Zurek mechanism [95, 96]. Different methods allow to observe several forms of quantized vortices such as single vortices [97], vortex lattices [98,99], vortex pairs and rings [100, 101].

We showed that the metric describing the fluctuations depends on the velocity of the fluid and we used a model defined in literature as the "draining bathtub model (DBT)" [14]. The model has both tangential and radial velocities which posses both the event horizon and the ergoregion, which will be discussed later in section 3.5. Before going into the velocities, it is useful to introduce some concepts in vortex dynamics. One of the futures to describe the behavior of the vortices is the vorticity, a vector field that describes a microscopic measure of the rotation at any point in the fluid, given by

$$\vec{\omega} = \nabla \times \vec{v}. \tag{3.42}$$

For a rigid body the vorticity is twice the angular velocity, Ω and given by, $\vec{\omega} = \nabla \times \vec{v} = \nabla \times (\vec{\Omega} \times \vec{r}) = 2\vec{\Omega}$. For an irrotational vortex, the vorticity should be zero, any particle would maintain the same orientation while moving in a circle around a vortex axis. Because the fluid velocity for the BEC defined as $\vec{v} = (\hbar/m)\nabla\Phi$ (3.14), associated with the gradient of the phase parameter , any flow is fundamentally restricted to be

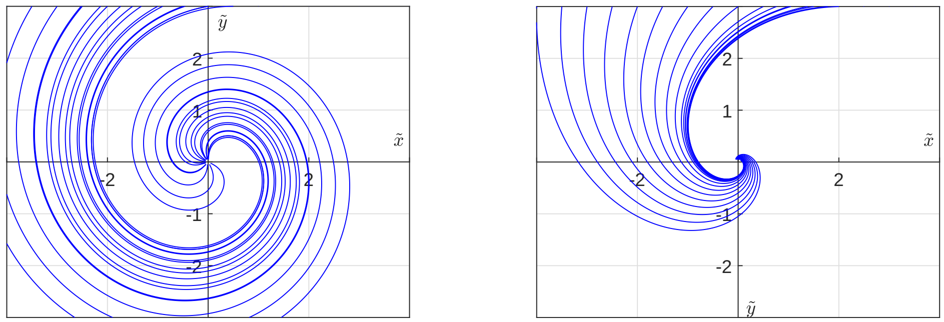

Figure 3.1: Streamlines of the vortex fluid for a single quantized vortex with winding number $q = 1$, for constant density (left) with velocity $\vec{v} = -\frac{A'}{r}\hat{r} + \frac{B'}{r}\hat{\theta}$ and self consistent density (right) with velocity $\vec{v} = -\frac{A}{\rho r}\hat{r} + \frac{B}{r}\hat{\theta}$. Parameters A, A' are calculated according to eqs. (3.73) and (3.76) and $B, B' = \hbar/m$ after the event horizon is set to 1 healing length.

irrotational (curl-free)

$$\nabla \times \vec{v} = \frac{\hbar}{m}\nabla \times \nabla\Phi = 0. \tag{3.43}$$

The circulation, denoted by Θ

$$\Theta = \oint \vec{v} \cdot \vec{dl} \tag{3.44}$$

is used to parametrized the fluid rotation. While classical vortices can take any value of the circulation, superfluids are irrotational, and any rotation or angular momentum is constrained to occur through vortices with quantized circulation [82]. This is a direct consequence of the fluid being associated with a macroscopic order parameter(wavefunction) $\psi = |\psi(r,t)|\, e^{i\Phi(r,t)}$. The circulation around a contour enclosing the vortex is non-vanishing and a multiple integer of the elementary circulation which gives the condition for tangential velocity,

$$\Theta = \oint \vec{v} \cdot d\vec{l} = 2\pi q \frac{\hbar}{m}, \quad q = \pm 1, \pm 2... \tag{3.45}$$

$$v_\theta = \frac{\Theta}{2\pi r}\hat{\theta}. \tag{3.46}$$

where r is the radius from the core and $\hat{\theta}$ is the azimuthal unit vector. For a single stable vortex $q = 1$ is chosen. Detail analysis will be given later. The radial part of the fluid velocity is calculated from continuity equation in cylindrical coordinates $\nabla \cdot (\rho\vec{v}) = 0$ with the vector identity, $\nabla \cdot (\rho\vec{v}) = \rho(\nabla \cdot \vec{v}) + \vec{v} \cdot (\nabla\rho)$ and ∇ in cylindrical coordinates

$$\rho\left(\frac{1}{r}\frac{\partial\left(rv_r\right)}{\partial r} + \frac{1}{r}\frac{\partial v_\theta}{\partial\theta} + \frac{\partial v_z}{\partial z}\right) + \vec{v} \cdot \left(\frac{\partial\rho}{\partial r}\hat{r}\frac{1}{r}\frac{\partial\rho}{\partial\theta}\hat{\theta} + \frac{\partial\rho}{\partial z}\hat{z}\right) = 0. \tag{3.47}$$

As stated above the tangential velocity is purely radial and keeping the density as a general form for 2D- vortex $\rho\left(r\right)$, the radial velocity becomes

$$\frac{\partial}{\partial r}\left(\rho\left(r\right)rv_r\right) = 0 \Rightarrow v_r = -\frac{A}{\rho(r)r}. \tag{3.48}$$

Here A is a positive constant to be determined, and the minus sign signifies the inward direction of the radial velocity of the fluid. Thus, the velocity of the vortex fluid becomes

$$\vec{v} = v_\theta + v_r = \frac{-A}{\rho(r)r}\hat{r} + \frac{B}{r}\hat{\theta} \tag{3.49}$$

where B is $\frac{\hbar}{m}$ from the Eq.3.46. One of the main assumption in the literature is the constant density approximation which forms the DBT model defined in [49], [14] with a velocity

$$\vec{v} = \frac{-A'}{r}\hat{r} + \frac{B'}{r}\hat{\theta} \tag{3.50}$$

where A' and B' are determined accordingly.

3.4.1 Density derivation of an unbound single vortex

We start with the GP equation (3.6), defined for weakly interacting bosons

$$i\hbar\frac{\partial\psi(x,t)}{\partial t} = \left(-\frac{\hbar^2}{2m}\nabla^2 + V_{ext} + U_0\left|\psi\right|^2\right)\psi(x,t). \tag{3.51}$$

In an unbounded condensate with $V_{ext} = 0$ the stationary solutions take the form $\psi(x,t) = \psi(x)e^{-i\mu t/\hbar}$. Known vortex solutions with a single winding number or index q in cylindrical coordinates can be written as

$$\psi(r,\theta) = f_q(r)e^{iq\theta}, \tag{3.52}$$

and the density is defined as $\rho(r) = \left|\psi(r,\theta)\right|^2$. Inserting the Eq.3.52 to the GP Eq.3.51 with the chemical potential μ (3.8), gives

$$\frac{4a\pi\rho\hbar^2}{m^2}f_m = -\frac{\hbar^2}{2m}\frac{1}{r}\frac{\partial}{\partial r}\left(r\frac{\partial f_m}{\partial r}\right) + \frac{\hbar^2}{2mr^2}f_q + U_0 f_q^3. \tag{3.53}$$

Here ρ represents the bulk density which in turns gives the bulk speed of sound Eq.3.10 and the healing length Eq.3.11. While we are calculating the radial dependent density, we assign the bulk value to the density at infinity ρ_∞. Therefore the equation above (3.53) presents a natural scaling factor, the healing length ξ, and defining a new variable $\chi_q = f_q/\sqrt{\rho_\infty}$ transforms the equation to a simple form:

$$\frac{1}{\tilde{r}}\frac{d}{d\tilde{r}}\left(\tilde{r}\frac{d\chi_q}{d\tilde{r}}\right) + \frac{\chi_q}{\tilde{r}^2} + \chi_q^3 - \chi_q = 0 \tag{3.54}$$

with the boundary conditions

$$\chi_q(0) = 0 \qquad\qquad \chi_q(\infty) = 1. \tag{3.55}$$

The functional form of χ_q near $r = 0$ and $r = \infty$ can be established directly from

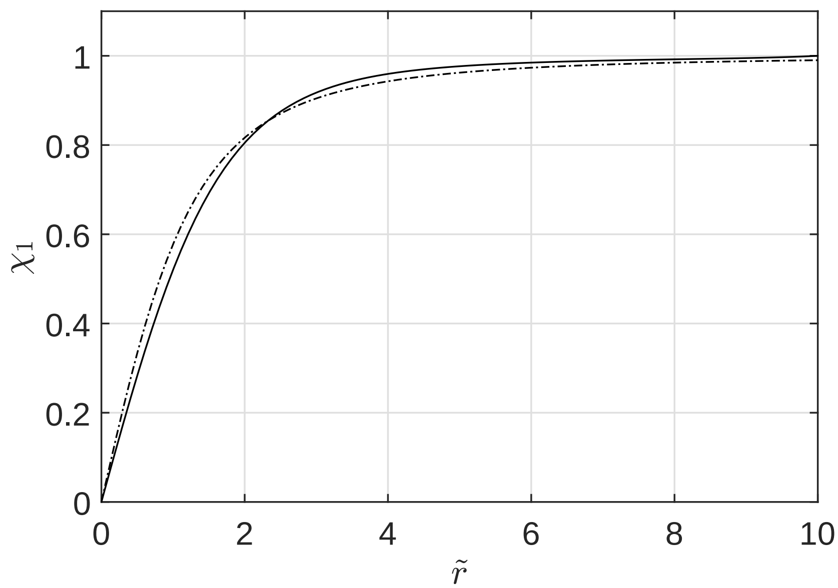

Figure 3.2: The radial wave function $\chi(\tilde{r})$ obtained by numerical solution of the stationary GP equation for a straight vortex line with the approximate form given in Eq.3.57 shown by a dashed line.

the equation by taking the appropriate limit;

$$\chi_q(r) = \begin{cases} \tilde{r}^{|q|} + \mathcal{O}(\tilde{r}^{|q|+2}) & \text{as } \tilde{r} \to 0, \\ \\ 1 - q^2/2\tilde{r}^2 + \mathcal{O}(1/\tilde{r}^4) & \text{as } \tilde{r} \to \infty. \end{cases} \tag{3.56}$$

The vortices with the winding numbers $q = \pm 1$ are found to be topologically stable, while the vortices with larger values of $|q|$ are considered to be unstable and should decay into single-charge vortices [102], [103]. Thus, Eq.3.54 is analyzed for $q = 1$ case. Fig.3.4 shows the numerical calculation of the equation 3.54 with the boundaries defined in Eq.3.55. For an unbound vortex, it shows that the density goes to its bulk value near $\approx 7\xi$. In addition, approximate analytical form is chosen which will be used in the calculations of superradiance and horizons [83], [104]. Analytical form is given by

$$\chi = \sqrt{\frac{\tilde{r}^2}{2 + \tilde{r}^2}}. \tag{3.57}$$

which in turn gives the density of the fluid and the speed of sound in most general form with the Eqs. 3.10-3.11

$$\rho_0(r) = \rho_\infty \frac{r^2}{r^2 + 2\xi^2}, \tag{3.58}$$

$$c(r) = c_\infty \sqrt{\frac{r^2}{r^2 + 2\xi^2}}, \tag{3.59}$$

where $c_\infty = \frac{\hbar}{m}\sqrt{4\pi a \rho_\infty}$, $\rho_\infty = \frac{1}{8\pi\xi^2 a}$ is the bulk density or density at infinity, ξ is the healing parameter.

3.5 Event horizon and Ergoregion

With fluid models, one can reproduce a wide variety of geometries with nontrivial causal structures. Here, we analyze an analogy that corresponds to rotating black holes, which posses two horizons; event horizon and ergosphere. The event horizon is an outer trap for light i.e point of no return. The analogue event horizon is created in a way that the fluid velocity overcomes the sound velocity at a specific boundary. Therefore inside the horizon, sound can not travel beyond and trapped in a region.

The second horizon is the ergosphere, and inside is defined as the ergoregion. The ergosphere, unlike the event horizon, occurs in rotating black holes only and defined as the region in which the spatial points move with superluminal velocity relative to a fixed star. Analogue ergosphere is defined by a much simpler way. A region where the speed of flow is greater than the speed of sound and equal to the speed of sound at the ergosphere. Differently from general spacetimes in GR, for acoustic analogues there is a preferred reference frame given by the laboratory spatial and time coordinates.

In particular, there is a natural definition of at rest, with respect to the lab, and there is a preferred lab time coordinate t. Moreover, when the flow is steady, the time translation Killing vector defined as

$$K^\mu \equiv (\partial/\partial t)^\mu = (1,0,0,0)^\mu, \tag{3.60}$$

and for our metric

$$g_{\mu\nu}(\partial/\partial t)^\mu(\partial/\partial t)^\nu = g_{tt}, \tag{3.61}$$

so that, the ergoregion is naturally defined as a region where the vector K becomes spacelike and an ergosurface is the surface where K is null. The sign of g_{tt} depends on the values of the speed of sound $c(r)$ and the velocity of the fluid υ. A change of sign in g_{tt} characterizes an ergoregion. In previous section 3.2.1, line element is calculated as

$$ds^2 = \frac{\rho(r)}{c(r)}\left[-c(r)dt^2 + (dr - \upsilon_r dt)^2 + (rd\theta - \upsilon_\theta dt)^2\right]. \tag{3.62}$$

In order to minimize the number of off-diagonal components of the metric which helps in analyzing the asymptotic behavior, thus to see the distinction between the event horizon and the ergosphere, a new coordinate system is introduced as;

$$dt = dt^* - \upsilon_r/\left(c^2 - \upsilon_r^2\right)dr, \tag{3.63}$$

$$d\theta = d\theta^* - \upsilon_r\upsilon_\theta/\left(r\left(c^2 - \upsilon_r^2\right)\right)dr, \tag{3.64}$$

$$r = r^*, z = z^*, \tag{3.65}$$

From now on, we drop the *-superscript and the final form is written as

$$ds^2 = \frac{\rho}{c}\left[\left(\upsilon^2 - c^2\right)dt^2 + \frac{c^2}{c^2 - \upsilon_r^2}dr^2 + r^2 d\theta^2 - 2\upsilon_\theta r dt d\theta\right]. \tag{3.66}$$

From the definitions explained above, as for the Kerr black hole in general relativity, the radius of the ergosphere is given by the vanishing of the coefficient dt^2, which is $\upsilon^2 - c(r)^2 = 0$. Negative g_{tt} indicates the timelike character of the time-coordinate, whereas positive g_{tt} is the space-like character.

$$\upsilon^2 - c(r)^2 < 0, \text{ supersonic flow, i.e ergoregion} \tag{3.67}$$

$$\upsilon^2 - c(r)^2 > 0, \text{ subsonic flow, outside of the ergosphere.} \tag{3.68}$$

The coordinate singularity of the metric, i.e the event horizon, occurs when $\upsilon_{\hat{r}}^2 - c(r)^2 = 0$. We can deduce from this definition that the event horizon must be either contained within or coincide with the ergosphere. For stationary black holes, i.e, purely radial flow, the ergosphere actually coincides with the event horizon, thus has a very little effect after all.

The presence of an ergoregion enables an important process called the Penrose process, which amounts to the extraction of energy by outside agents from the rotational energy of a black hole. Analogue of the Penrose process here that allows particles to carry more energy coming out from a black hole is called the superradiance, that is the main focus of our research and is discussed in detail in section 4.

3.5.1 Derivation of the event horizon and the ergoregion for a DBT model with a constant density profile

The constant density approximation is widely used in the calculation of the superradiance effect in DBT models. The velocity of the fluid given as

$$\vec{\upsilon} = \frac{-A'}{r}\hat{r} + \frac{B'}{r}\hat{\theta} \tag{3.69}$$

and by following the coordinate transformations in eqs. (3.63) to (3.65), the new coordinates are

$$dt^* = dt - \frac{A'r}{A'^2 - c^2r^2}dr, \tag{3.70}$$

$$d\theta^* = d\theta - \frac{A'B'}{r(A'^2 - c^2r^2)}dr \tag{3.71}$$

with $r = r^*$ and$z = z^*$. We drop the *-superscript in the following part of the formulation. The line equation takes the form

$$ds^2 = \frac{\rho_0}{c}\left[-\left(1 - \frac{A'^2 + B'^2}{c^2r^2}\right)dt^2 + \left(1 - \frac{A'^2}{c^2r^2}\right)^{-1}dr^2 - \frac{2B'd\theta dt}{c} + r^2d\theta^2 + dz^2\right]. \tag{3.72}$$

The event horizon, r'_h, and the ergosphere, r'_e, can be identified termwise in the metric now. The radius of the ergosphere is given by the vanishing of g_{tt} and the coordinate singularity of the metric signifies the event horizon;

$$r'_h = A'/c, \qquad r'_e = (A'^2 + B'^2)^{1/2}/c > r'_h. \tag{3.73}$$

3.5.2 Derivation of the event horizon and the ergoregion for an unbound single vortex with a self consistent density profile

Using the same method, with velocity the defined in Eq.3.49, the density ρ in Eq.3.58, and the speed of sound in Eq.3.59, the new coordinates take the form of

$$dt^* = dt - \frac{Ar^3(r^2 + 2\xi^2)^2}{c_\infty^2\rho_\infty r^8 - A^2(r^2 + 2\xi^2)^3}dr, \tag{3.74}$$

$$d\theta^* = d\theta - \frac{ABr(r^2 + 2\xi^2)^2}{c_\infty^2\rho_\infty r^8 - A^2(r^2 + 2\xi^2)^3}dr \tag{3.75}$$

with $r = r^*$ and$z = z^*$. Now we can calculate the location of the ergosphere when $v^2 - c^2 = 0$ and the coordinate singularity of the metric, i.e the event horizon, when

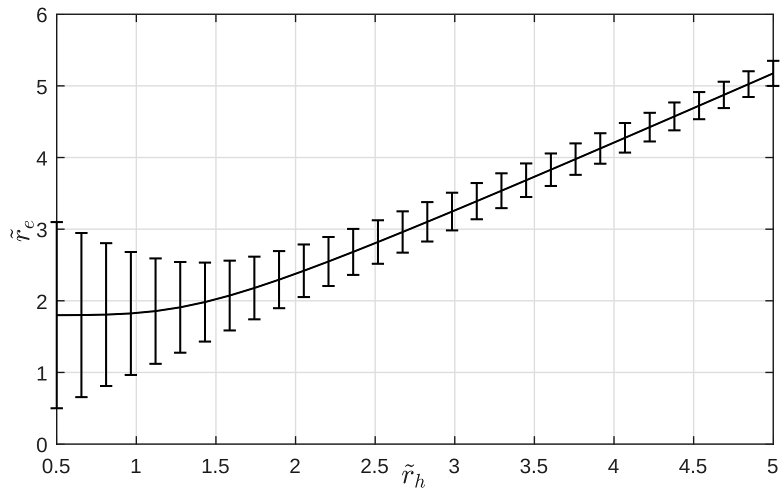

Figure 3.3: Representation of the ergosphere vs the event horizon for a single vortex with $B = \hbar/m$ and $A = c\,(r_h)\, r_h \rho\,(r_h)$, vertical bars show the radial length of the ergoregion, $\tilde{r}_e - \tilde{r}_h$.

$\upsilon_{\hat{r}}^2 - c^2 = 0$. These conditions read respectively as

$$\frac{A}{\rho_\infty c_\infty} - \frac{r_h^4}{\left(r_h^2 + 2\xi^2\right)^{3/2}} = 0, \tag{3.76}$$

$$\frac{A^2\left(r_e^2 + 2\xi^2\right)^2}{\rho_\infty^2 r_e^6} + \frac{B^2}{r_e^2} - \frac{c_\infty^2 r_e^2}{r_e^2 + 2\xi^2} = 0. \tag{3.77}$$

From the two equations above we can set a relation between the ergosphere and the event horizon for a single vortex with $B = \hbar/m \equiv \sqrt{2} c_\infty \xi$;

$$\frac{r_h^8}{\left(r_h^2 + 2\xi^2\right)^3}\frac{\left(r_e^2 + 2\xi^2\right)^2}{r_e^6} + \frac{2\xi^2}{r_e^2} - \frac{r_e^2}{r_e^2 + 2\xi^2} = 0. \tag{3.78}$$

The relation is solved numerically, showing that the ergosphere is getting narrow by the increasing event horizon shown in Fig.3.3. Numerical calculations showed that after $r_h \approx 2.5\xi$, there is no superradiance since the ergoregion is considerably small for the wave to extract enough energy during propagation. Which sets an upper

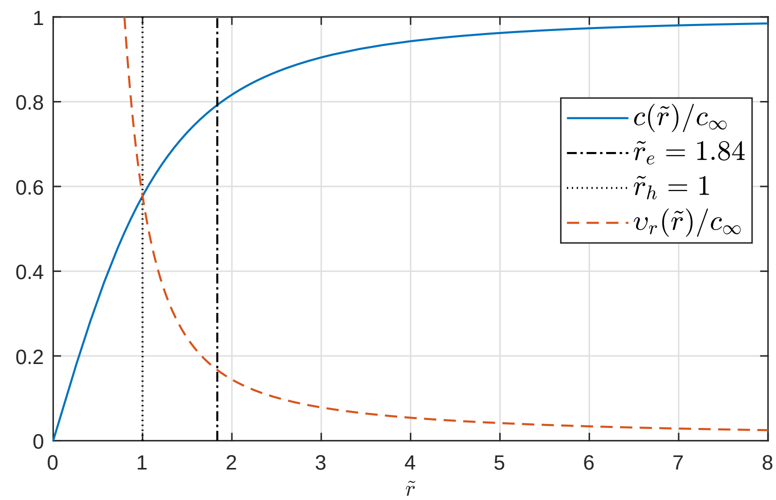

Figure 3.4: The event horizon, r_h, the ergoregion, r_e, the speed of sound, $c(r)$ and the radial velocity of the fluid, $\upsilon_r(r)$ as a function of radial distance from the vortex center.

boundary for the event horizon value in the case of an unbound vortex with self consistent background density. While these restrictions can be overcome to some extent by an external potential, in our case ($V_{ext} = 0$), the event horizon has to be near healing length. After the event horizon, r_h is set to 1ξ, the constant A reads as $\frac{\xi\rho_\infty c_\infty}{3^{3/2}}$ and the constant B is $\hbar/m$ from the definition Eq.3.46. In order to compare the variables we used the parameters of the Bose-Einstein condensate produced in a rubidium-87 gas given as [105], [79];

$$a = 5.77nm \qquad\qquad m = 1.44 * 10^{-25}kg \qquad\qquad \rho_\infty = 10^{21}m^{-3}$$

These numbers lead to values for the speed of sound at the infinity, $c_\infty = 6.2\times10^{-3}m/s$ and healing length $\xi = 8.3\times10^{-8}m$. We can now numerically calculate the ergoregion from Eq.3.77, which gives 8 roots with only 1 positive, real root $r_e = 1.84\xi$. Fig.3.4 shows the velocities as scaled with speed of sound away from the vortex c_∞, and the lengths scaled with the healing length ξ, $\tilde{r} = r/\xi$.

3.6 Discussion

1D- flow of a condensate with a sonic horizon as an analogy for black holes has been achieved experimentally [44] and considering the slow nature of the sound propagation and the low temperature of the condensate, it presents an opportunity to observe the desired effects. The 2D vortex structure of a Bose-Einstein condensation also presents an analogy for black holes with both horizons under the hydrodynamic approximation. While experimentally it may be challenging, we showed here in a theoretical point, both the event horizon and the ergoregion are present in the DBT model with the radial and the tangential velocities accordingly. In our case, we analyzed a single unbound vortex with a winding number $q = 1$ and numerically calculated the radial dependent density form. Later, the density formalization is used to calculate the corresponding event horizon and the ergosphere of the black hole analogy.

Chapter 4

ANALOG SUPERRADIANCE

The superradiance phenomena was first suggested by Zel'dovich in 1971 [10]. Zel'dovich pointed out that a cylinder made of an absorbing material, rotating around its axis with angular velocity Ω, can amplify incident waves with angular frequency ω, provided the condition

$$\omega < m\Omega \tag{4.1}$$

is satisfied, where m is the azimuthal quantum number with respect to the rotation axis. Energy extraction from black holes was first introduced by Roger Penrose [106]. The idea was based on a particle with initial energy decays into two particles and since the energy of a particle within ergoregion can be negative relative to an observer at infinity, the observed particle can have energy bigger than the initial energy due to energy conservation (For a general review [107]). It is important to note that even though superradiance is usually called the wave-counterpart of the Penrose process, they are two different features. Any rotating body with internal degrees of freedom can display superradiance as long as it has absorbing features, i.e a region where energy can be dumped into. When spacetime is curved, superradiance can also occur in vacuum, the existence of a horizon provides the dissipative mechanism that is necessary for superradiance [108, 109]. Therefore, the Penrose process does not need an event horizon but only an ergoregion, while superradiance needs a certain horizon where the negative energy particles should be confined in.

The scattering problem in a traditional sense defined as

$$\frac{d^2 f}{dx^2} + \left(\omega^2 + V(x)\right) f = 0, \tag{4.2}$$

here ω is interpreted as frequencies and the solution to the wave, f, consist of incoming, transmitted and outgoing solutions such as;

$$\mathcal{I}e^{ik_{in}x} + \mathcal{R}e^{ik_r x} \quad x \to +\infty, \tag{4.3}$$

$$\mathcal{T}e^{ik_t x} \quad x \to -\infty, \tag{4.4}$$

where k_{in}, k_r and k_t are the momenta and $\mathcal{I}, \mathcal{T}$ and $\mathcal{R}$ are the coefficients of incident, reflected and transmitted waves respectively, which are obtained by the dispersion relation;

$$-k_{in,r}^2 + \omega^2 + V(x \to +\infty) = 0, \tag{4.5}$$

$$-k_t^2 + \omega^2 + V(x \to -\infty) = 0. \tag{4.6}$$

The conservation of the Wronskian of the solutions to Eq. 4.2, $W[f]$

$$1 - |\mathcal{R}|^2 = -\frac{k_t}{k_r}|\mathcal{T}|^2, \tag{4.7}$$

gives a condition for the superradiance, $|\mathcal{R}|^2 > 1$, in certain cases depending on the $V(x)$. The formulation can be applied to gravitational waves scattering from equatorial Kerr metric [110], electromagnetic radiation scattering on a rotating cylinder [111],wave scattering form Bose Einstein condensates.

4.1 Experimental Detection of Superradiance

For Kerr Black holes, the process is still purely kinematic, depends on the rotation of objects and it is taking place in the background spacetime. Compared to the spontaneous Hawking radiation, the effect is stronger and the stimulated nature simplifies the attempts to determine whether an analogue system in a laboratory setting will manifest it or not. The first detection report was announced by Quantum Gravity Laboratory in Nottingham. The experiment was performed on a surface of water with a draining bathtub fluid flow. The plane waves were amplified after being scattered and %20 amplification was recorded [40, 45]. Also, alternative methods have been presented such as using a rotating cylinder to mimic the vortex for the scattering of sound waves [55].

Chapter 5

NUMERICAL ANALYSIS OF SUPERRADIANCE

In this chapter, the two main assumptions; the constant density and the non-constant, self consistent density profile, given in Eq.3.58 are analyzed in both time and frequency domains. In the first part 5.1, we applied a numerical method mostly presented in [85, 112, 113] in order to transform the second order partial differential equation, the KG equation 3.34, into the first order set of equations by using the line equation 3.66, which are much easier to handle numerically. After, in section 5.2.1, the first approximation, the constant density, is applied to the equation set and the propagation of the phase fluctuation Φ_1 is analyzed in the time domain. Thus the energy of the wave and the reflection coefficients are calculated. In section 5.2.2, the Eq.3.34 is solved in the frequency domain, which shows the superradiance condition by analyzing the asymptotic solutions of the wave equation. Also the reflection coefficient is calculated for different ranges of rotational frequencies of the fluid and the frequency of the incident wave. We compare the two different methods to solve Eq. 3.34, and analyze the reflections coefficients of the scattered wave. In the section 5.3.1, the second assumption, the self consistent density profile, is used to analyze the wave propagation in both time (Sec.5.3.1) and the frequency (Sec.5.3.2) domains.

5.1 Derivation of the Field Equations

The KG equation

$$\frac{\partial}{\partial t}\left[\frac{\rho_0}{c^2}\left(\frac{\partial \Phi_1}{\partial t}+\vec{v}_0\cdot\nabla\Phi_1\right]\right)-\nabla\cdot(\rho_0\nabla\Phi_1)+\nabla\cdot\left[\frac{\rho_0}{c^2}\left(\frac{\partial \Phi_1}{\partial t}+\vec{v}_0\cdot\nabla\Phi_1\right)\upsilon_0\right]=0, \quad (5.1)$$

can be written in explicit form in cylindrical coordinates

$$\Bigg[\frac{\partial^2}{\partial t^2} + 2\upsilon_r \frac{\partial^2}{\partial t \partial r} + \frac{2\upsilon_\theta}{r}\frac{\partial^2}{\partial t \partial \theta} + \left(-c^2 + \upsilon_r^2\right)\frac{\partial^2}{\partial r^2} + \frac{2\upsilon_\theta \upsilon_r}{r}\frac{\partial^2}{\partial r \partial \theta}$$
$$+ \left(-\frac{c^2}{r^2} + \frac{\upsilon_\theta^2}{r^2}\right)\frac{\partial^2}{\partial \theta^2} + \frac{1}{r}\frac{\partial (r\upsilon_r)}{\partial r}\frac{\partial}{\partial t} + \left(-\frac{\upsilon_\theta \upsilon_r}{r^2} + \frac{\upsilon_\theta}{r}\frac{\partial \upsilon_r}{\partial r}\right)\frac{\partial}{\partial \theta}$$
$$+ \left(-\frac{c^2}{r} - \frac{c^2}{\rho}\frac{\partial \rho(r)}{\partial r} + \frac{\upsilon^2}{r} + 2\upsilon_r \frac{\partial \upsilon_r}{\partial r} + \upsilon_\theta \frac{\partial \upsilon_\theta}{\partial r}\right)\frac{\partial}{\partial r} - c^2 \frac{\partial^2}{\partial z^2}\Bigg]\Phi_1 = 0, \tag{5.2}$$

and a line element written as

$$ds^2 = -\alpha^2 dt^2 + \gamma_{ij}(dx^i + \beta^i dt)(dx^j + \beta^j dt), \tag{5.3}$$

where $\alpha = c$, $\gamma_{ij} = diag(1, r^2, 1)$ and $\beta^i = (-\upsilon_r, -\upsilon_\theta/r, 0)$. Two conjugate fields are introduced accordingly:

$$\Gamma = \frac{\partial \Phi_1}{\partial x^i} \qquad\qquad \Pi = -\frac{1}{c}\left(\frac{\partial \Phi_1}{\partial t} - \beta^i \Gamma_i\right), \tag{5.4}$$

where $x_i = (r, \theta, z)$ denote the cylindrical coordinates and $\beta^i = (-\upsilon_r, -\upsilon_\theta/r, 0)$ are the velocity components. The fields are introduced formally as

$$\Phi_1 = \phi_1(t,r)e^{im\theta}e^{ikz} \qquad \Pi = \pi_1(t,r)e^{im\theta}e^{ikz} \qquad \Gamma = \gamma_1(t,r)e^{im\theta}e^{ikz} \tag{5.5}$$

with (k, m) denoting the axial and azimuthal wave numbers [114]. We can also calculate the density fluctuations given in Eq.3.33, in terms of the conjugate fields;

$$\frac{\rho_1}{\sqrt{2}\rho_0 \xi} = -\frac{1}{c}\left[\frac{\partial \Phi_1}{\partial t} - \upsilon_0 \cdot \nabla \Phi_1\right] = \Pi \tag{5.6}$$

In this work, in accordance with the single BEC vortex stability conditions, azimuthal wave number m is chosen as $m = 1$ and $m = 0$ (non-superradiant condition) [102], [103]. In addition $k = 0$ is chosen for the translational symmetry along the z axis. Three coupled first order partial differential equations are obtained by using the conjugate fields Γ, Π, Φ_1 (detailed derivation given in appendix C);

$$\frac{\partial \phi_1}{\partial t} = -c\pi_1 - \upsilon_r \gamma_1 - \frac{im\upsilon_\theta}{r}\phi_1, \tag{5.7}$$

$$\frac{\partial \gamma_1}{\partial t} = -\frac{\partial c}{\partial r}\pi_1 - c\frac{\partial \pi_1}{\partial r} - \frac{\partial \upsilon_r}{\partial r}\gamma_1 - \upsilon_r\frac{\partial \gamma_1}{\partial r} - \frac{\partial \upsilon_\theta}{\partial r}\frac{im}{r}\phi_1 + \frac{im\upsilon_\theta}{r^2}\phi_1 - \frac{im\upsilon_\theta}{r}\frac{\partial \phi_1}{\partial r}, \tag{5.8}$$

$$\begin{aligned}\frac{\partial \pi_1}{\partial t} =& \pi_1\left(-\frac{\partial c}{\partial r}\frac{\upsilon_r}{c} - \frac{im\upsilon_\theta}{r} - \frac{1}{r}\frac{\partial (r\upsilon_r)}{\partial r}\right) + \frac{\gamma_1}{c}\left(-\frac{c^2}{r} - \frac{c^2}{\rho}\frac{\partial \rho}{\partial r} + \frac{\upsilon_\theta^2}{r} + \upsilon_\theta\frac{\partial \upsilon_\theta}{\partial r}\right) \\ & - \upsilon_r\frac{\partial \pi_1}{\partial r} - c\frac{\partial \gamma_1}{\partial r} + \frac{\phi_1}{c}\left(\frac{m^2c^2}{r^2} + c^2k^2 - \frac{im\upsilon_r}{r}\frac{\partial \upsilon_\theta}{\partial r} - \frac{im\upsilon_r\upsilon_\theta}{r^2}\right).\end{aligned} \tag{5.9}$$

Here the density, ρ, the speed of sound, c, and the fluid velocity, υ, are functions of radial distance. Now the equation set is first order and much more easy to handle than the KG equation(5.2).

5.1.1 Boundaries of the simulation

Our radial domain includes the event horizon r_h, which is a condition for superradiance phenomena to occur. Therefore, the numerical boundary should be placed inside the horizon. However, in theory, no information should leave the event horizon. This allows us to implement a technique called the "black-hole excision" by allowing the wave to propagate inside the horizon and excise its interior from the computational domain and removing the coordinate singularity r_h and the singularity $r = 0$. The excision technique is adopted from Ref.s [115] and [113]. Therefore, the inner boundary is chosen as a free boundary where the wave propagates inside freely and removed from the computational domain later by tracking the event horizon for any outgoing waves during the simulations. The outer boundary is constructed from the null rays (see appendix A), that shows the outgoing and the incoming fields along the null ray in terms of conjugate fields

$$U^{\mu}_{out}\partial_{\mu}\Phi_1 + \propto \Gamma - \Pi, \qquad\qquad U^{\mu}_{in}\partial_{\mu}\Phi_1 + \propto \Gamma + \Pi. \tag{5.10}$$

The simulation is terminated before reaching the outer boundary so that any reflection or unphysical wave is prevented. For the outer boundary, this translates to $U^{\mu}_{out}\partial_{\mu}\Phi_1 = 0$, therefore $\Gamma = \Pi$. The initial wave is set far from the vortex, so it is not affected and the reflection coefficient and the energy of the wave are measured at the same location by tracking the reflected wave. Therefore both the radial and the time domains are chosen accordingly, and the time domain is large enough that the wave can reach at least the starting point and the radial domain is large enough that the final reflected wave is entirely inside the domain. In order to check the simulation accuracy, the constrained value, C, is evaluated at the event horizon and the selected final position of the wave, which is from the Eq.5.4

$$C = \left| \frac{\partial \phi_1}{\partial r} - \pi_1 \right|, \tag{5.11}$$

and the biggest violation occurs at the event horizon which is still under the accepted range as shown in the next section 5.2.1. Consequently, constraint violations at the event horizon start to interfere with the physical computation domain when the time domain is chosen too large. Therefore simulation time has to be chosen according to the constraint violation as well.

5.2 Simulation of the Superradiance in BEC for a Constant Density Approximation

5.2.1 Numeric analysis in the time domain under a constant background density

The constant density, thus the constant speed of sound approximation, is one of the most common methods in superradiance research. Although when defining a vortex, the DBT fluid flow, density of the fluid at the center of the vortex should be nearly zero, considering the vortex core is sufficiently small compared to the wavelength of the scattered wave, we expect the result should not be too far off. Starting with the fluid velocity in Eq.3.69, eqs. (5.7) to (5.9) is written as

$$\partial_t \pi_1 + c\partial_r \gamma_1 - \frac{A'}{r}\partial_r \pi_1 = -imB'\pi_1/r^2 + c(k^2 + m^2/r^2)\phi_1 - c\gamma_1/r, \tag{5.12}$$

$$\partial_t \phi_1 - \frac{A'}{r}\partial_r \phi_1 = -imB'\phi_1/r^2 - c\pi_1, \tag{5.13}$$

$$\partial_t \gamma_1 + c\partial_r \pi_1 - \frac{A'}{r}\partial_r \gamma_1 = 2imB'\phi_1/r^3 - (A' + imB')\gamma_1/r^2. \tag{5.14}$$

Scaled parameters are selected via the event horizon for distances and the speed of sound for the velocity. We assign the event horizon to a making, $A' = ac$ according to the Eq.3.73 and the angular frequency of the vortex defined at the event horizon as $\vec{v_\theta} = \vec{\Omega} \times \vec{r}$, gives the constant $B' = \Omega a^2$. Thus for the simulations the scaled radial coordinate is $\tilde{r} = r/a$ and the time coordinate is $\tilde{t} = tc/a$, and the resulted frequencies are scaled by $\tilde{\omega} = \omega a/c$, $\tilde{\Omega} = \Omega a/c$

The eqs. (5.12) to (5.14) are integrated numerically using Matlab PDE solver by modifying equation format and boundary conditions accordingly (Sec.5.1.1).The computational spatial (radial) and time domain are set as $0.2 < \tilde{r} < 150, 0 < \tilde{t} < 150$, with discretization steps of $\Delta\tilde{r} = 0.05$, $\Delta\tilde{t} = 0.05$, respectively. The domain is sufficiently large to achieve steady state solutions, whereas the discretization steps provide good accuracy for the solution.

$$\phi_1(0, r) = Nexp\left[-(r - r_0 + ct)^2/b^2 - i\omega(r - r_0 + ct)/c\right]. \tag{5.15}$$

The radial part of the incident wave is an axisymmetric imploding Gaussian pulse modulated by a monochromatic wave, centered at r_0 with a width of b. Here, c is the speed of sound in the condensate. N is calculated by the normalization of the incident wave on the radial domain. Initial equations for the wave π_1 and γ_1 are calculated from the definitions 5.4.

Fig.5.1 and Fig.5.2 show the propagation of the wave at specific times for non-

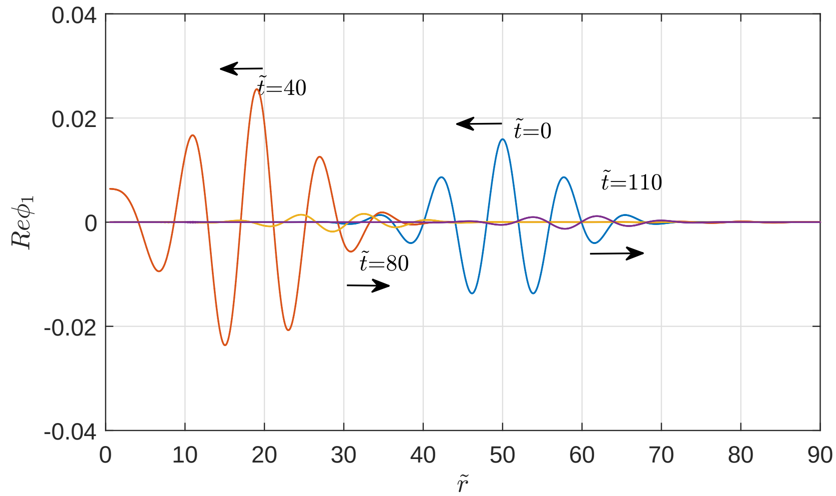

Figure 5.1: Snapshots of the time evolution of the perturbation, for the case m=0 as a function of distance $\tilde{r}$ from the vortex, for $r_0 = 50a$ and $b = 10a$ with $\omega = 0.7c/a$, $\Omega = 1.4c/a$

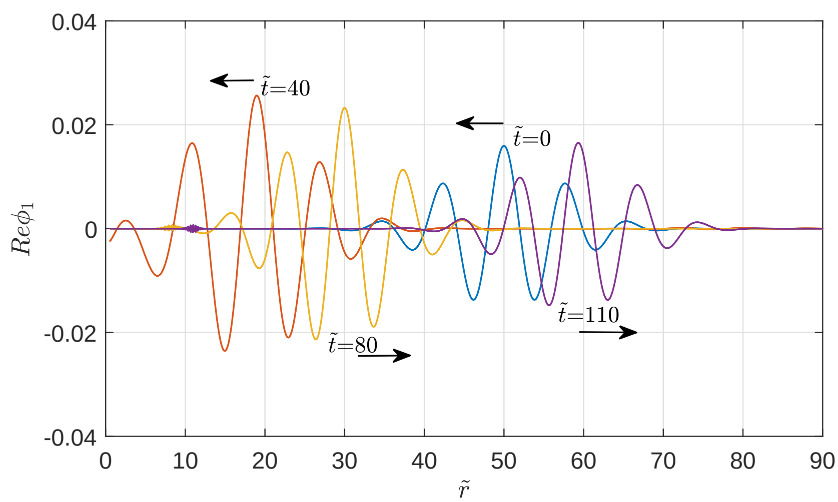

Figure 5.2: Snapshots of the time evolution of the perturbation, for the case m=1 as a function of distance r from the vortex. The parameters used are in Fig. 5.1

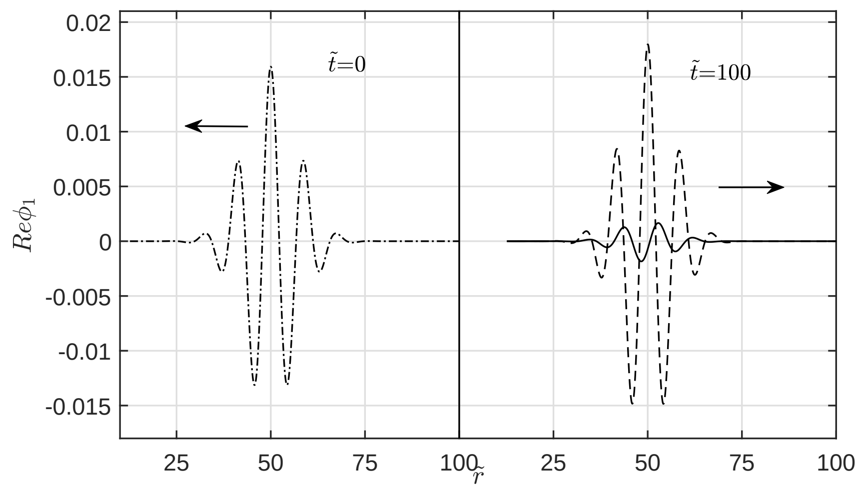

Figure 5.3: Incident wave(t=0) and the reflected wave($t = 100a/c$) for the superradiance case, amplified(dotted line) and non superradiant case. The parameters used are $r_0 = 50a$ and $b = 10a$ with $\omega = 0.7c/a$, $\Omega = 1.4c/a$

superradiant case $m = 0$ and the superradiant case $m = 1$, respectively. In the superradiant case wave is amplified, while for non-superradiant case goes to zero as expected. In order to see the amplification clearly, the incident and the reflected wave has to be analyzed at the same location. Fig.5.3 shows the side by side comparison of the wave measured at the initial point $r_0 = 50a$. The reflected wave reaches the start point around $\tilde{t} = 100$.

Constraint violations $C = |\partial_r \phi_1 - \gamma_1|$, explained in Sec.5.1.1, are monitored during the simulation in order to check the validity of the numerical result. To analyze the constraint violations at the outer boundary we choose $r = 70a$ and record the wave at this location, as well as the event horizon as our inner boundary. While the violations are recorded at $r = 70a$, the simulation boundary is much larger. However, since the reflected wave can not reach the outer boundary of the simulation at a given time, the monitor is positioned at an earlier point. The constraint violations at the event horizon (left panels) and at the outer boundary $r = 70a$ (right panels) are shown in Figures 5.4 and 5.5 for superradiant and non-superradiant cases. As expected, the violations are much larger when the wave passes through a selected position.

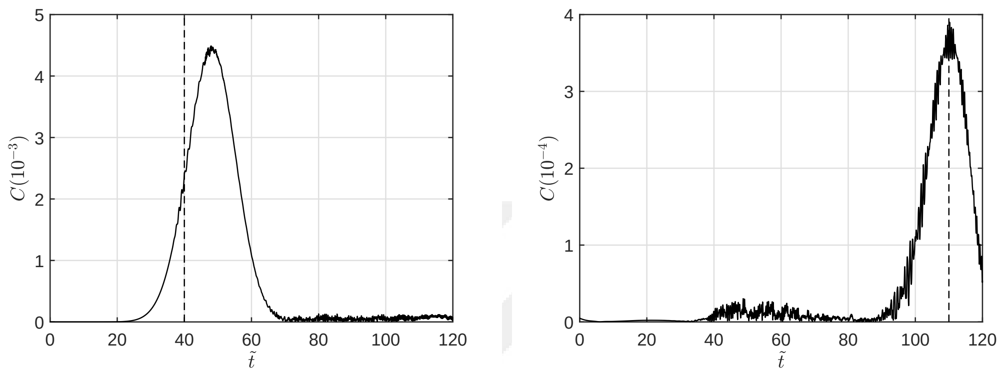

Figure 5.4: Constraint violations at event horizon(a) and outer boundary ($\tilde{r} = 70$)(b) for superradiance (m=1). The parameters used are in Fig. 5.1. Dotted lines signify the time frames($\tilde{t} = 40, 110$), when the wave reaches the horizon and the outer boundary

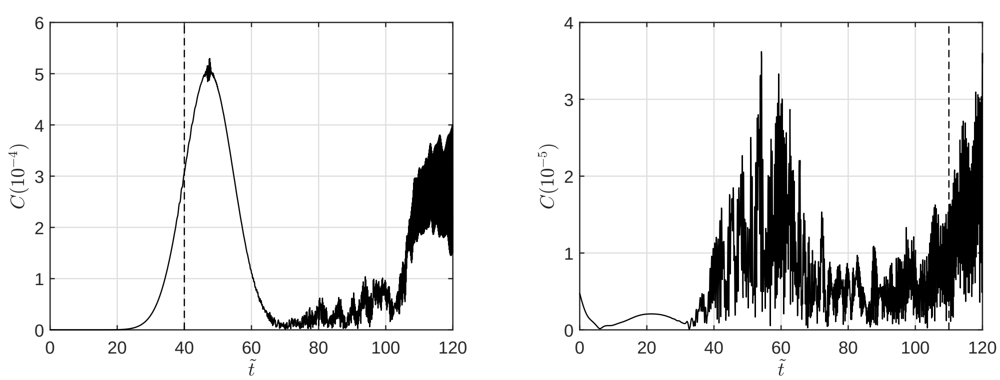

Figure 5.5: Constraint violations at event horizon(a) and outer boundary($\tilde{r} = 70$)(b) for non-superradiance (m=0). The parameters used are in Fig. 5.1

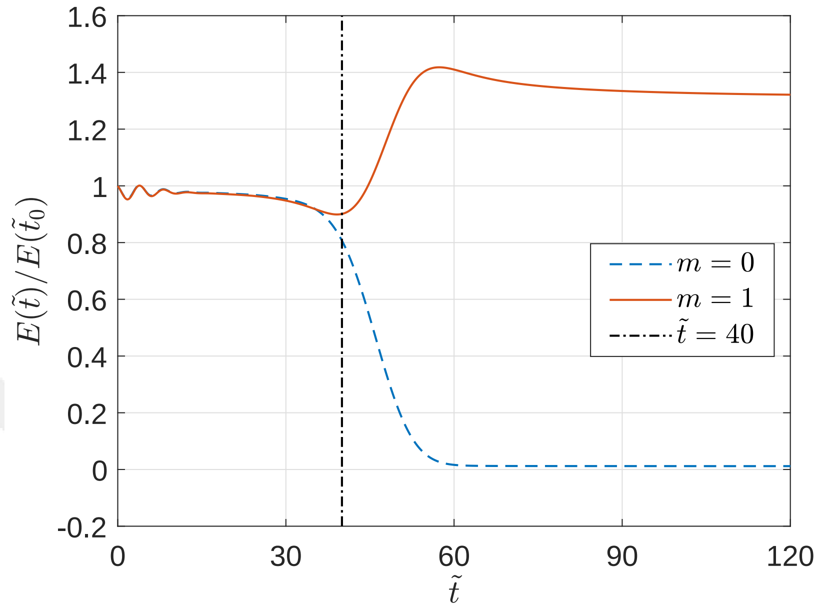

Figure 5.6: Time evolution of the wave energy normalized to its initial value for superradiant m=1 case and non-superradiant m=0 case. The parameters used are in Fig. 5.1

In addition, the magnitude of the constraint violations is observed to be an order of magnitude higher at the event horizon than the outer boundary. Fig.5.5(a) also shows that after the wave left the horizon, there are still instabilities induced at the boundary as well as the inside the region where the excision technique applied and removed from the computational domain. Fig.5.2 also shows at later times $\tilde{t} = 80$ and $\tilde{t} = 100$, at the left side of the wave tail there are small instabilities escaping the event horizon which can be seen from the constraint evolution as well. While the main wave Gaussian pulse is not disturbed by the effect, numerical analysis has to be kept in check for outgoing unphysical waves from the horizon. If the simulation time kept much longer, unphysical waves may propagate further and render the simulation results obsolete. While the figures only show the constraint violations at a specific rotational frequency, Ω, as well as the wave frequency, ω, our analysis shows that for larger rotational frequency simulations become unstable faster and especially at the event horizon magnitude of constraint increases significantly. Finally, the energy

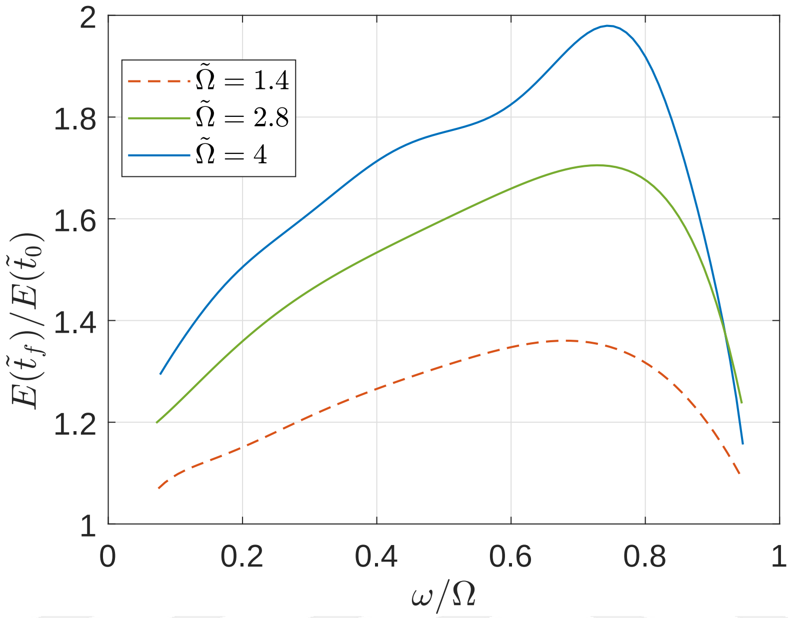

Figure 5.7: The Energy of the wave normalized to its initial value as a function of ω/Ω where $0 < \omega < \Omega_i$.The parameters used in the calculations are $\Omega_i = 1.4c/a$, $2.8c/a$, $4c/a$, $r_0 = 50a$, $b = 10a$. Energy values recorded when the outgoing wave reached the initial position at $r = 50a$.

associated with the superfluid flow, the energy of the wave packet, is calculated from

$$E(t) = \int \partial^3 r \frac{1}{2} M\rho\vec{v}^2 = (\rho\hbar^2/2M) \int_0^{2\pi} d\phi \int_0^H dz \int_1^{r_{max}} (\nabla\psi_1)^2 r dr. \tag{5.16}$$

Fig.5.6 shows the initialized energy for the non-radiant (dashed blue curve) and superradiant (solid red curve) cases respectively. And the horizontal line represents the approximate time the wave reaches the horizon. Almost %32 energy gain is observed for superradiant case with parameters $\Omega = 1.4c/a$ and $\omega = 0.7c/a$.

For different rotational frequencies, the amplification of energy as a function of the relative center frequency of the wave ω/Ω is plotted in Fig.5.7, which shows the change in the behavior when the rotational frequency is increased. The maximum energy gain is in the range $0.6 < \omega/\Omega < 0.8$ and there is a rapid decrease when $\omega/\Omega \approx 1$ as expected from the superradiant condition $\omega < m\Omega$. It is important

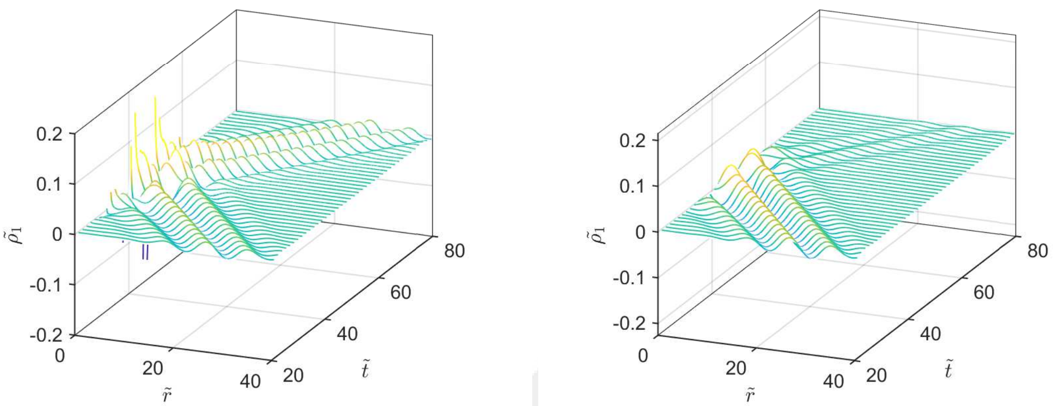

Figure 5.8: Density fluctuations, ρ_1, calculated according to Eq.5.6 and scaled as $\tilde{\rho_1} = \rho_1/\xi\rho_0$ in r-t plane for superradiance case, m=1 (left) and m=0 (right).The parameters used in the calculations are given in Fig.5.1.

to note that for the constant density approximation we used we have the freedom to increase the fluid rotational frequency as an independent variable. However as explained in Sec.5.3.1, that is not the case for self consistent BEC vortex density profile.

Fig.5.8 shows the time evolution of the density fluctuations for superradiant and non superradiant cases. Here sudden increase in the density fluctuation for the superradiant case lies inside the event horizon, $r = 1a$. In cylindrical coordinates density fluctuation is shown in Fig.5.9 at a specific time $t = 100a/c$.

5.2.2 Numeric analysis in the frequency domain under constant background density

Second method to study superradiance is to analyze the Klein Gordon equation 5.2 in the frequency domain. To start, the solution of KG equation is written by the separation of variables in the form of

$$\Phi_1 = e^{-i\omega t} e^{im\theta} e^{ikz} P(r), \tag{5.17}$$

where k and m are the axial and azimuthal wave numbers, respectively. k is defined by the boundary conditions along the z axis which taken as zero, considering that the

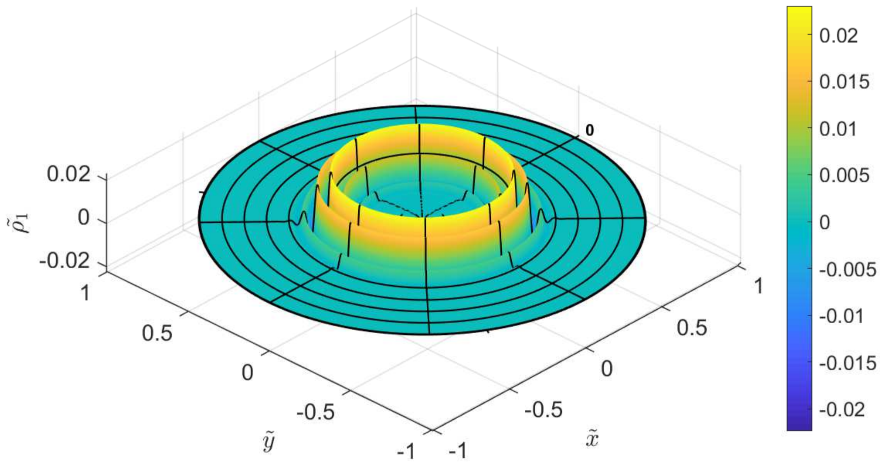

Figure 5.9: Scaled density fluctuations $\tilde{\rho}_1 = \rho_1/\xi\rho_0$, in cylindrical coordinates at time $\tilde{t} = 100$ for superradiant case. The parameters used in the calculations are given in Fig.5.1.

wave propagation along z axis is non-existing.

By inserting 5.17 into 5.2, with the fluid velocity defined as $\upsilon = -A'/r + B'/r$ for the constant density approximation, we obtain a second order ODE for the radial part:

$$\frac{d^2P}{dr^2} + \left(\frac{A'^2 + r^2c^2 + 2iA'(B'm - r^2\omega)}{r(r^2c^2 - A'^2)}\right)\frac{dP}{dr}$$

$$+ \left(\frac{2iA'B'm - B'^2m^2 + c^2m^2r^2 + 2B'm\omega r^2 - r^4\omega^2 + c^2k^2r^4}{r^2(r^2c^2 - A'^2)}\right)P = 0. \tag{5.18}$$

In order to eliminate the event horizon, coordinate change in the radial domain is introduced to map the event horizon to $-\infty$ which is called Regge-Wheeler tortoise coordinate shown as r_*, which will map $r \in [r_H, \infty]$ to $r_* \in [-\infty, +\infty]$:

$$r_* = \int \frac{r^2}{r^2 - A'^2/c^2}dr. \tag{5.19}$$

After, the wave equation can be written as $P = R(r)H(r_*)$. Introducing r_* into Eq.5.18 gives the final form of the equation for $H(r_*)$

$$\frac{d^2H(r_*)}{dr_*{}^2} + \left(\frac{\omega^2}{c^2} - V(r)\right)H(r_*) = 0, \tag{5.20}$$

where

$$V = k^2(1-\frac{A'^2}{r^2c^2}) - \frac{5A'^4}{4c^4r^6} - \frac{A'^2\left(m^2-3/2\right)+B'^2m^2}{c^2r^4} - \frac{1}{4r^2c^2}\left(c^2-4m^2c^2-8B'\omega\right). \tag{5.21}$$

Before solving the equation above, asymptotic behavior can be analyzed. At the asymptotics $r \to \pm\infty$ solutions behaves as harmonic functions;

$$H(r_*) = e^{\frac{-i\omega_+ r_*}{c}} + \mathcal{R}\mathrm{e}^{\frac{+i\omega_+ r_*}{c}}, r^* \to +\infty, \tag{5.22}$$

$$H(r_*) = \mathcal{T}e^{\frac{-i(\omega-\Omega m)r_*}{c}}, r^* \to -\infty, \tag{5.23}$$

where $\omega_+^2 = \omega^2 - k^2c^2$ and $\Omega = B'/a^2$ and $\mathcal{R}(\mathcal{T})$ are the amplitudes of the reflected (transmitted) waves, respectively. Here, ω_+^2 needs to be positive in order to achieve scattering states. While we kept the constant k during the calculations, for the numerical analysis $k = 0$ is used. Solutions at asymptotics and their complex conjugates are independent from each other and their Wronskian is can be calculated as $y_1 = H(r_*)$ and $y_2 = H^*(r_*)$, where H^* is the complex conjugate of H,

$$W\left(\pm\infty\right) = y_1\dot{y_2} - y_2\dot{y_1}, \tag{5.24}$$

$$W\left(+\infty\right) = \frac{2i\omega_+}{c}\left(1-\left|\mathcal{R}^2\right|\right), \tag{5.25}$$

$$W\left(-\infty\right) = \frac{2i\left(\omega - m\Omega\right)}{c}\left(1-\left|\mathcal{T}^2\right|\right). \tag{5.26}$$

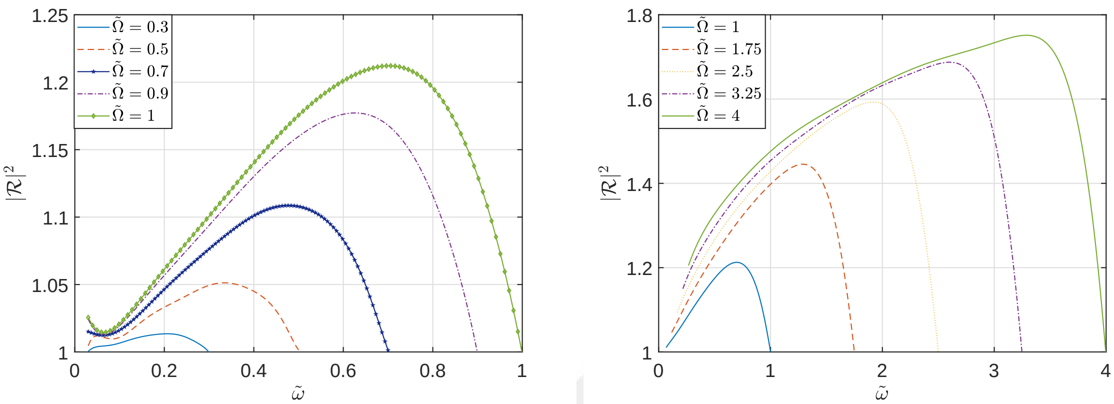

Figure 5.10: Reflection coefficients as a function of ω, calculated in the range $0 < \omega < m\Omega_i$. Parameters are $m = 1$, $\Omega_i a/c =$0.3, 0.5, 0.7, 0.9, 1 (right) and $\Omega_i a/c =$1, 1.75, 2.5, 3.25, 4 (left)

Since the Wronskian of these solution at asymptotic should be equal to each other, $W(+\infty) = W(-\infty)$, we reach a relation between the reflection and the transmission coefficients $(\mathcal{R}, \mathcal{T})$,

$$1 - |\mathcal{R}|^2 = \left(\frac{\omega - m\Omega}{\omega_+}\right) |\mathcal{T}^2| \tag{5.27}$$

which shows the reflection coefficient has a magnitude larger than unity when the superradiance condition $\omega < m\Omega$ is satisfied [116], [117].

While we reach the superradiance condition by analyzing the asymptotic behavior, in order to solve the Eq.5.20, we implement a method which solves the Eq.5.19 and Eq.5.19 simultaneously and calculate the Fourier components of the solution at asymptotic to analyze the incoming and outgoing waves. Fig.5.18 shows the behavior of the reflection coefficients for a specific rotational frequency, while the Fig.5.11 shows the full spectrum. Here we employ the same values for the parameters (m, a, c, k, A, B) with the time domain calculations in order to check the compatibility. Figure 5.18 shows that for $\Omega > 1$ and $\Omega < 1$, reflection coefficient behavior is slightly changing. After we have the full spectrum, we can analyze the maximum reflection coefficient as a function of rotational frequency and the wave frequency. Fig.5.12(a) shows the

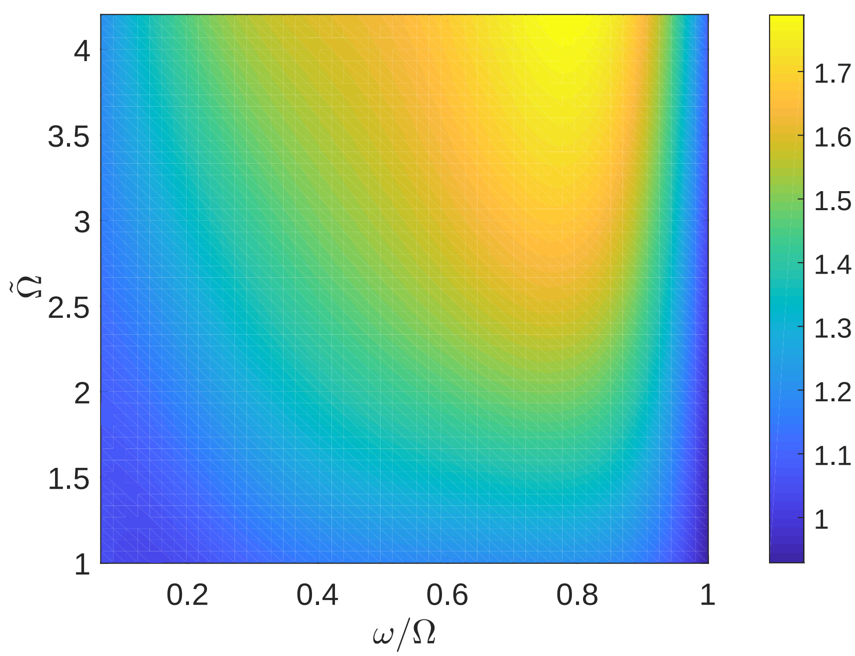

Figure 5.11: Full spectrum of reflection coefficient values between $1 < \Omega a/c < 4.2$ calculated in the range $0 < \omega < m\Omega_i$

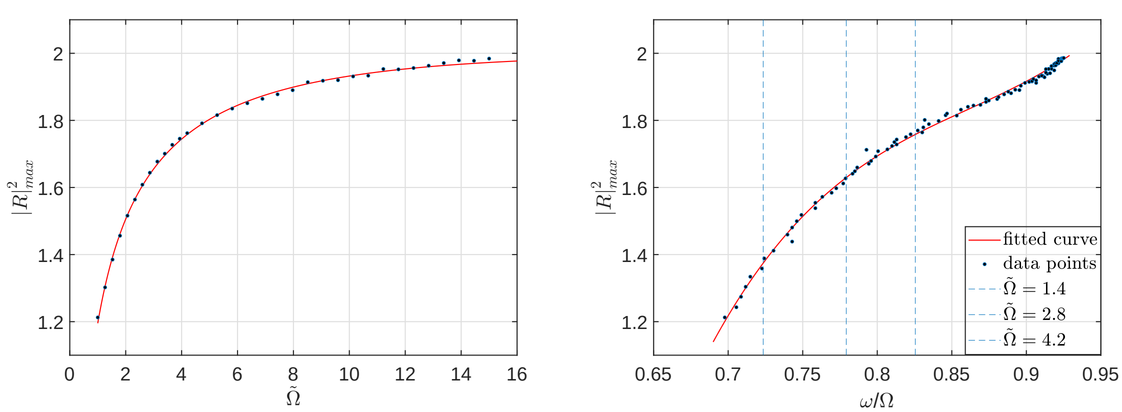

Figure 5.12: Maximum reflection coefficient behavior with respect to Ω between $1 < \Omega a/c < 16$ (right) and with respect to ω/Ω between $1 < \Omega a/c < 16$(left).

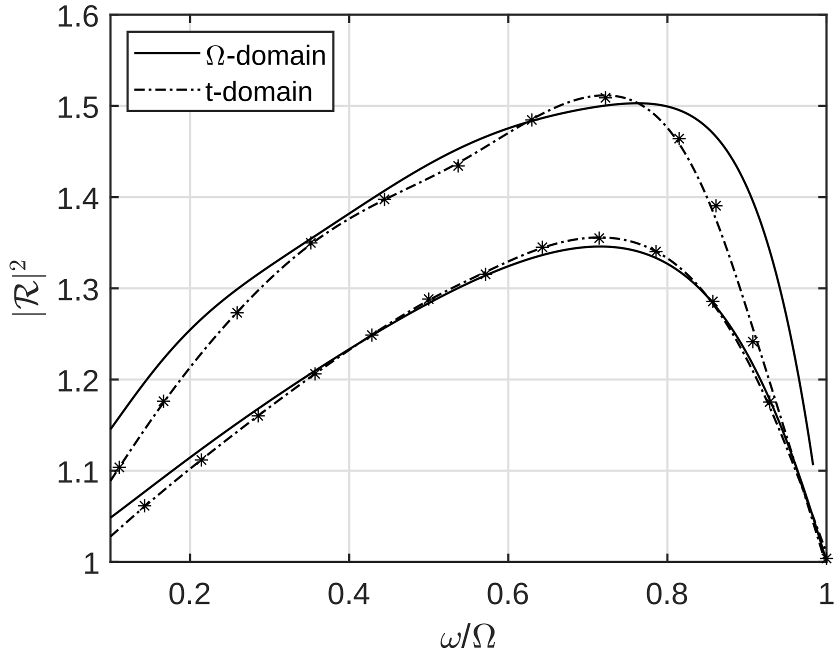

Figure 5.13: Reflection coefficients of the scattered wave with parameters given under Fig.1 calculated in the time domain and the frequency domain for $\Omega = 1.4c/a$ and $\Omega = 2.8c/a$

maximum value of the reflection coefficient as a function of Ω rotational frequency of the vortex. It shows an upper bound for the maximum amplification, which might be connected to entropy bound as stated in [107]. Fig.5.12(b) shows the maximum reflection coefficient achieved with respect to the ratios of the frequencies also shows that there is a pile up just below the reflection coefficient two and the maximum amplification appears to be achieved around $\omega/\Omega. \approx 0.93$. However, the stability of the vortex at large frequencies is an another important issue, Thus in theory, while we can increase the vortex rotational fluid, how much reliable are the results is a significant question. Finally, we can compare the two methods we applied to solve the Eq.5.2. We analyzed the refection coefficients in both domains keeping the parameters, such as $m, k, \Omega, \omega, a, c$, same. Fig.5.13 compares the reflection coefficients calculated in the time domain and the frequency domain, for different values of Ω. At $\Omega = 1.4c/a$, the agreement is very good while for larger rotational frequencies, we start to observe different behaviors. As stated in the time domain calculations, for larger Ω simulations become unstable much faster. This may be the reason for the differences in the calculations.

5.3 Simulation of Superradiance in BEC for Self Consistent Background Density Approximation

5.3.1 Numeric analysis in the time domain under self consistent background density

Now we have a single vortex with a density profile, Eq.3.57, derived from the GP equation 3.6 with known vortex solutions of the background $\psi_0 = \sqrt{\rho_0} e^{i\Phi_0}$ with first order fluctuations $\psi = \psi_0 + \psi_1 = \sqrt{\rho} e^{i\Phi}$. The constant A calculated from Eq.3.76 after setting the event horizon to one healing length and the constant B is calculated from 3.46 for a single vortex with winding number $q = 1$,

$$A = \frac{\rho_\infty c_\infty \xi}{3\sqrt{3}}, \qquad B = \frac{\hbar}{m} = \sqrt{2} c_\infty \xi. \tag{5.28}$$

The fluid velocity for a single stable vortex Eq.3.49 and the speed of sound can be written explicitly as

$$\vec{v} = \frac{-A}{\rho(r) r}\hat{r} + \frac{B}{r}\hat{\phi} = -\frac{\xi c_\infty}{3\sqrt{3}} \frac{r^2 + 2\xi^2}{r^3}\hat{r} + \frac{\sqrt{2} c_\infty \xi}{r}\hat{\phi}, \tag{5.29}$$

$$c\,(r) = c_\infty \sqrt{\frac{r^2}{r^2 + 2\xi^2}}. \tag{5.30}$$

Length parameters are scaled with the healing length. Note that, the scaling factor is not a free parameter, since in order to achieve the density profile (3.57) from the Eq.3.54 lengths must be scaled with healing length. Otherwise the density profile must be changed accordingly. Second, the velocity parameters are scaled with the speed of sound at infinity and the scaled velocities become;

$$\vec{\tilde{v}} = \frac{\sqrt{2}}{\tilde{r}}\hat{\phi} - \frac{1}{3\sqrt{3}}\frac{\tilde{r}^2+2}{\tilde{r}^3}\hat{r}, \tag{5.31}$$

$$\tilde{c} = \sqrt{\frac{\tilde{r}^2}{\tilde{r}^2+2}}. \tag{5.32}$$

The eqs. (5.7) to (5.9) for the given speed of sound and the fluid velocity are;

$$\frac{\partial \phi_1}{\partial \tilde{t}} = -\frac{\tilde{r}}{\sqrt{\tilde{r}^2+2}}\pi_1 + \frac{\tilde{r}^2+2}{3\sqrt{3}\tilde{r}^3}\gamma_1 - \frac{im\sqrt{2}}{\tilde{r}}\phi_1, \tag{5.33}$$

$$\begin{aligned}\frac{\partial \gamma_1}{\partial \tilde{t}} =& -\frac{2}{\left(\tilde{r}^2+2\right)^{3/2}}\pi_1 - \frac{\tilde{r}}{\sqrt{\tilde{r}^2+2}}\frac{\partial \pi_1}{\partial \tilde{r}} - \frac{\tilde{r}^2+6}{3\sqrt{3}\tilde{r}^4}\gamma_1 - \frac{\tilde{r}^2+2}{3\sqrt{3}\tilde{r}^3}\frac{\partial \gamma_1}{\partial \tilde{r}} \\ &+ \frac{2\sqrt{2}im}{\tilde{r}^3}\phi_1 - im\sqrt{2}\frac{\partial \phi_1}{\partial \tilde{r}},\end{aligned} \tag{5.34}$$

$$\begin{aligned}\frac{\partial \pi_1}{\partial \tilde{t}} =& \pi_1\left(\frac{im\sqrt{2}}{\tilde{r}^2} - \frac{2}{3\sqrt{3}\tilde{r}^4}\right) - \frac{\tilde{r}^2+2}{3\sqrt{3}\tilde{r}^3}\frac{\partial \pi_1}{\partial \tilde{r}} - \left(\frac{1}{\sqrt{\tilde{r}^2+2}} + \frac{4\tilde{r}+\tilde{r}^3}{\tilde{r}\left(\tilde{r}^2+2\right)}\right)\gamma_1 \\ &- \frac{\tilde{r}}{\sqrt{\tilde{r}^2+2}}\frac{\partial \phi_1}{\partial \tilde{r}} + \left(\frac{m^2\tilde{r}^2}{\tilde{r}^3\sqrt{\tilde{r}^2+2}}\right)\phi_1.\end{aligned} \tag{5.35}$$

The same methodology with the constant density approximation is used. The equation set is integrated numerically by Matlab's PDE solver toolbox with an FDTD solver. The computational domain is chosen as $0.5 < r/\xi < 110$ for spatial (radial) and $0 < tc_\infty/\xi < 110$ for time whereas the discretization step is 0.05 for both cases. Boundaries are selected with same procedure; i.e at large distances, purely outgoing waves which corresponds to $\pi - \gamma = 0$, and free inner boundary inside the event horizon. Simulation is stopped before wave reaches the outer boundary. Accuracy of the simulation is checked by constraint evolution defined in Eq.5.11 at the event

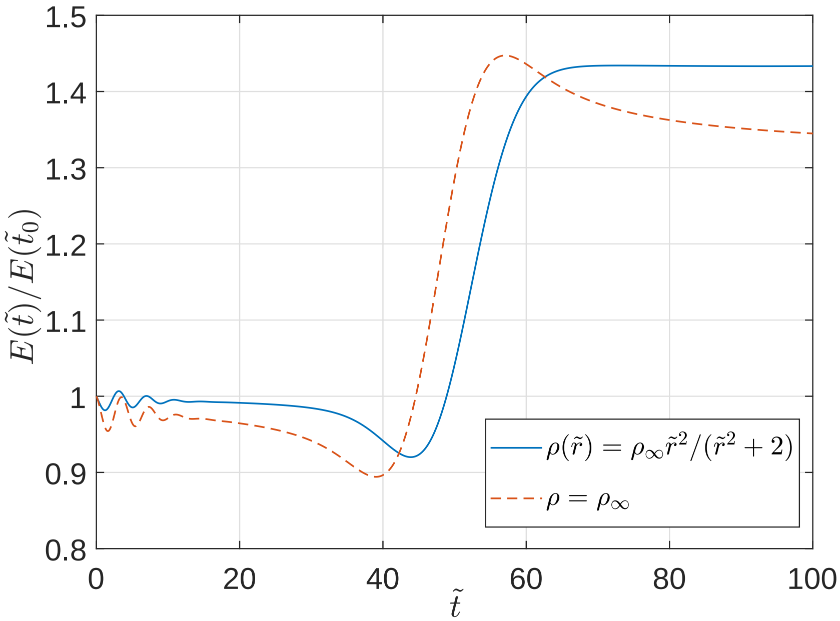

Figure 5.14: Time evaluation of the energy gain of the wave packet for superradiant case for constant and non-constant density profiles. Wave parameters used are $r_0 = 50\xi$ and $b = 10\xi$ with $\omega = 0.8c_\infty/\xi$

horizon and at a specific position chosen to be monitored during calculations.

$$\phi_1(0,r) = Aexp\left[-(r - r_0 + c(r)t)^2/b^2 - i\omega(r - r_0 + c(r)t)/c(r)\right]. \tag{5.36}$$

The incident wave is chosen as a cylindrically imploding Gaussian wave, centered at r_0 with a width of b and the initial values for π_1 and γ_1 are calculated according to Eq.5.4.

With the non constant speed of sound c, the velocity of the perturbation changes on the radial domain. And the energy of the scattered wave is calculated using

$$E(t) = (\hbar^2/2M)\int_0^{2\pi} d\phi \int_0^H dz \int_1^{r_{max}} \rho(r)(\nabla\Phi_1)^2 r dr. \tag{5.37}$$

The figure 5.14 shows the time evolution of the energy of the wave, normalized by its initial value for the two main assumptions, the constant density and the non-constant

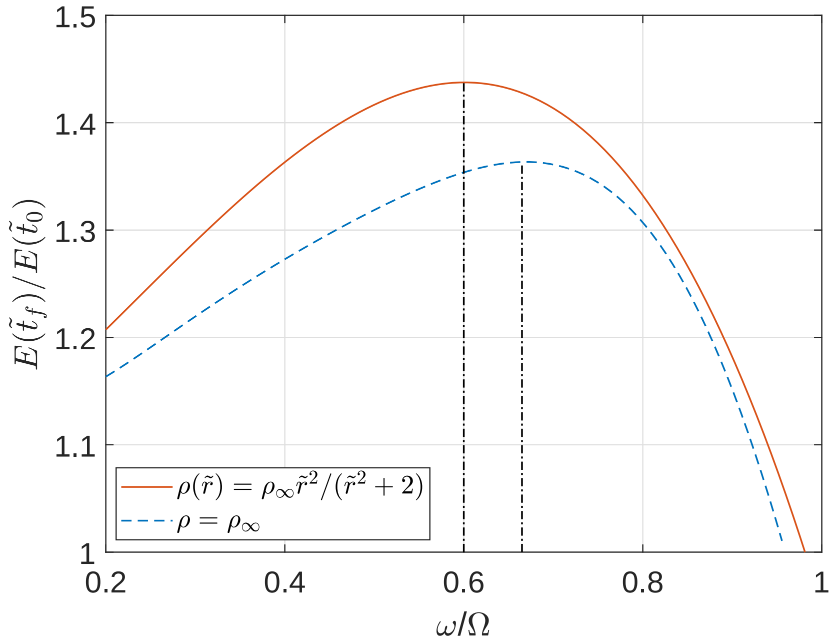

Figure 5.15: Energy gain difference between constant density and non-constant density approach for $\tilde{\Omega}/5 < \tilde{\omega} < \tilde{\Omega}$. Parameters given in Fig.5.14

density. Here for the comparison event horizon is set to 1ξ and the initial wave parameters r_0, b and ω are the same in both cases. However, since the behavior of density and the speed of sound differ, the radial velocity of the fluid and the location of the ergosphere are different. For the non-constant density case, the wave reaches the vortex at a later time, considering the speed of sound, $c(r)$ gets slower closes to the vortex core. In addition, we observe that the energy of the reflected wave reaches a steady value much faster after leaving the vortex. And an extra $\approx \%8$ energy gain, compared to the initial energy, is observed.

Fig.5.15 shows the energy ratios between two assumptions analyzed in the region of $\sqrt{2}c_\infty/5\xi < \omega < \sqrt{2}c_\infty/\xi$. Upper boundary for ω is set using the defined rotational velocity of the BEC. For an irrotational flow rotational frequency behavior defined as $\Omega \propto 1/r^2$ such that $\vec{v}_{\hat{\phi}} = \vec{\Omega} \times \vec{r}$. Superradiance condition is shown as $\omega < m\Omega$, where Ω corresponds to the rotational frequency at the event horizon. Given the value for

B, the rotational frequency of the vortex becomes

$$\Omega = \frac{B}{r_h^2} = \sqrt{2}c_\infty/\xi. \tag{5.38}$$

Compared to the constant density approximation, a higher energy gain is calculated, for a single value of rotational frequency, since the Ω is quantized and for a single stable vortex density profile 3.57 shapes the radial velocity with the scaling parameter 1ξ. Therefore, we do not have the freedom to increase the rotational frequency or try different $q > 1$ values without changing the density profile, hence effecting the eqs. (5.7) to (5.9).

5.3.2 *Numeric analysis in the frequency domain under self consistent background density*

We again start by writing the Klein-Gordon equation (5.2) with a formal solution of the form

$$\Phi_1 = P(r)e^{i(m\theta-\omega t)}i \tag{5.39}$$

$$\frac{\partial^2 P(r)}{\partial^2 r} + Q(r)\frac{\partial P(r)}{\partial r} + Z(r)P(r) = 0, \tag{5.40}$$

where

$$Q(r) = \left(\frac{2im\upsilon_r\upsilon_\theta}{r} - 2i\omega\upsilon_r - \frac{\upsilon^2 - c^2}{r} - \frac{c^2}{\rho}\frac{\partial\rho}{\partial r} + \frac{\partial}{\partial r}\left(\upsilon_r^2 + \frac{\upsilon_\theta^2}{2}\right)\right)\frac{1}{\upsilon_r^2 - c^2}, \tag{5.41}$$

$$Z(r) = \left(\frac{2m\omega\upsilon_\theta}{r} - \omega^2 - m^2\frac{\upsilon_\theta^2 - c^2}{r^2} - \frac{i\omega}{r}\frac{\partial(r\upsilon_r)}{\partial r} - \frac{im\upsilon_\theta\upsilon_r}{r^2} + \frac{im\upsilon_\theta}{r}\frac{\partial\upsilon_r}{\partial r}\right)\frac{1}{\upsilon_r^2 - c^2}. \tag{5.42}$$

Tortoise coordinates defined in the same fashion to map the event horizon to $-\infty$, i.e $r \in [r_h, \infty]$ unto $r_* \in [-\infty, \infty]$

$$\Delta = \frac{dr_*}{dr} = \left(1 - \frac{\upsilon_r^2}{c^2}\right)^{-1} \tag{5.43}$$

Next, the radial part of the solution is expressed by the product of two functions one in tortoise coordinate and one in r, $P(r) = H(r_*)R(r)$, where introducing $P(r)$ into Eq.5.40 gives two equations

$$\frac{\partial R(r)}{\partial r} + M(r)R(r) = 0, \tag{5.44}$$

and

$$\frac{\partial^2 H(r_*)}{\partial r_*^2} + V(r)H(r_*) = 0. \tag{5.45}$$

The solution of Eq.5.44 is given by

$$R(r) = C\left(\frac{r^2 + 2\xi^2}{r^3}\right)^{1/2} exp\left(i\int h(r)dr\right) \tag{5.46}$$

where

$$h(r) = \frac{\upsilon_r\left(\upsilon_\theta - r\omega\right)}{r\left(\upsilon_r^2 - c^2\right)}, \tag{5.47}$$

and C is an arbitrary constant and the exponential part in the Eq.5.46 is rather complicated integration that we do not have to solve it completely. Eq.5.45 is the time-independent Schrodinger equation with

$$V(r) = \frac{1}{\Delta^2}\left(-\frac{\partial M}{\partial r} + M^2 - QM + Z\right), \tag{5.48}$$

$$M(r) = \left(\frac{Q}{2} + \frac{1}{2\Delta}\frac{\partial \Delta}{\partial r}\right), \tag{5.49}$$

where $V(r)$ reads explicitly

$$\begin{aligned} V(r) = &\left(\frac{\omega}{c} - \frac{m\upsilon_\theta}{rc}\right)^2 + \frac{(\upsilon_r^2 - c^2)\,\upsilon_r^2\,(5r^4 + 76r^2\xi^2 + 180\xi^4)}{4c^4r^2(r^2+2\xi^2)^2} \\ &+ \frac{(\upsilon_r^2 - c^2)\left(4m^2\left(r^2+2\xi^2\right)^2 - r^4 - 20r^2\xi^2 + 12\xi^4\right)}{4c^2r^2\left(r^2+2\xi^2\right)^2}. \end{aligned} \tag{5.50}$$

Detailed derivation is given in the Appendix B. The first term above can be considered as the energy term, including the energy of the wave and the rotational energy of the fluid such that we can write $V(r) = E(r,\omega) + V_1(r)$. Inserting the scaled velocity (Eq.5.31) and the scaled speed of sound (Eq.5.32), we can express $V(r)$ in dimensionless form,

$$V(\tilde{r},\tilde{\omega}) = E(\tilde{r},\tilde{\omega}) + V_1(\tilde{r}), \tag{5.51}$$

where

$$E(\tilde{r},\tilde{\omega}) = \frac{1}{\xi^2}\left(\frac{\tilde{r}^2+2}{\tilde{r}^2}\left(\tilde{\omega} - \frac{m\tilde{\Omega}}{\tilde{r}^2}\right)^2\right) \tag{5.52}$$

$$\begin{aligned} V_1(\tilde{r}) = -&\left(\left(-27\tilde{r}^8 + \tilde{r}^6 + 6\tilde{r}^4 + 12\tilde{r}^2 + 8\right)\left(2768\tilde{r}^2 + 2032\tilde{r}^4 + 696\tilde{r}^6 + 430\tilde{r}^8\right.\right. \\ &\left.\left.-535\tilde{r}^{10} - 27\tilde{r}^{12} + 108m^2\tilde{r}^8\left(\tilde{r}^2+2\right) + 1440\right)\right)/(2916\xi^2\tilde{r}^{18}(\tilde{r}^2+2)^2). \end{aligned} \tag{5.53}$$

Fig.5.16(a) and Fig.5.17(a) show the behavior of $V(\tilde{r_*},\tilde{\omega})$ with respect to scaled radial domain for $m=1$ and $m=0$, respectively, which shows that the ordering of the $\tilde{\omega}$-level curves at either end of the range are reversed in superradiant case while for

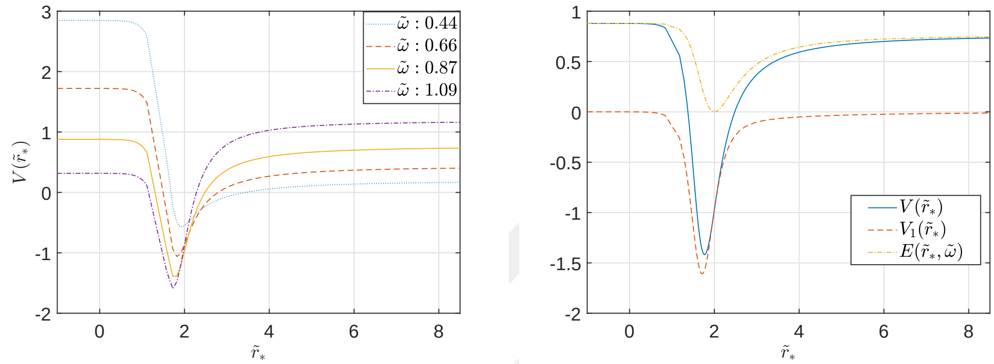

Figure 5.16: The radial behavior of $V(\tilde{r_*}, \tilde{\omega})$ for $\tilde{\omega} = 0.44, 0.66, 0.87, 1.09$, and behaviors of $E(\tilde{r}, \tilde{\omega})$,$V_1(\tilde{r})$ at fixed $\tilde{\omega} = 0.87$ for $m = 1$

.

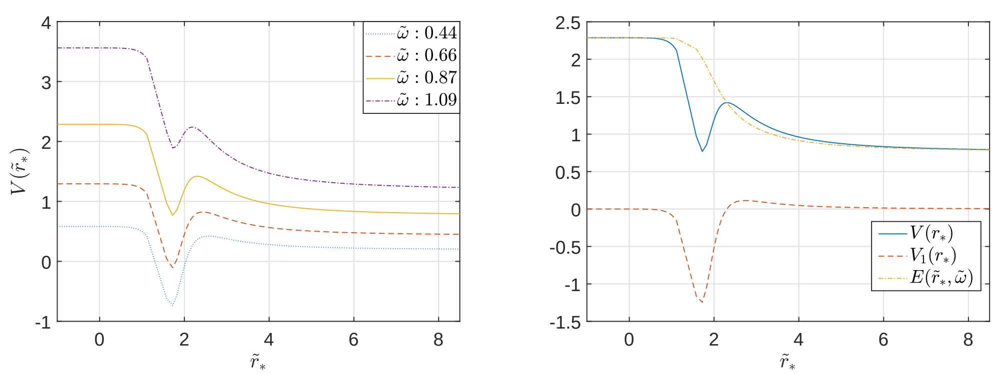

Figure 5.17: The radial behavior of $V(\tilde{r_*}, \tilde{\omega})$ for $\tilde{\omega} = 0.44, 0.66, 0.87, 1.09$, and behaviors of $E(\tilde{r}, \tilde{\omega})$,$V_1(\tilde{r})$ at fixed $\tilde{\omega} = 0.87$ for $m = 0$.

non-superradiant regime is just shifted. Fig.5.16(b) and Fig.5.17(b) show the three terms of Eq.5.51 separately for a fixed value of $\tilde{\omega} = 0.87$. Curiously, we observed that the maximum amplification is in fact occurs when the asymptotic values of $V(\tilde{r_*})$ are the same, i.e, $V(\tilde{r_*} \to +\infty) = V(\tilde{r_*} \to -\infty)$. The asymptotic values of $V(\tilde{r}, \tilde{\omega})$;

$$V(\tilde{r} \to 1, \tilde{\omega}) = 3\left(\tilde{\omega} - m\tilde{\Omega}\right)^2 / \xi^2, \tag{5.54}$$

$$V(\tilde{r} \to +\infty, \tilde{\omega}) = \tilde{\omega}^2 / \xi^2, \tag{5.55}$$

are equal to each other, with the condition that $\omega < m\Omega$, when $\tilde{\omega}$ is

$$V(\tilde{r} \to 1, \tilde{\omega}) = V(\tilde{r} \to +\infty, \tilde{\omega}), \tag{5.56}$$

$$\tilde{\omega}_{\pm} = m\tilde{\Omega}\frac{(6 \pm \sqrt{12})}{4}, \tag{5.57}$$

$$\tilde{\omega}_{-} = 0.63 m\tilde{\Omega} = 0.9, \tag{5.58}$$

and the value correlates with the simulations exactly. Major difference between two cases is the dip that occurs between the event horizon and the ergoregion in the behavior of $E(\tilde{r_*}, \tilde{\omega})$ for the superradiant case in contrast to the non-superradiant case which has monotonically increasing form the asymptotic to the event horizon.

Returning to the massless scalar field in Eq.5.39 we have

$$\Phi_1 = \left(\frac{r^2 + 2\xi^2}{r^3}\right)^{1/2} H(r_*) e^{i(m\theta - \omega t) e^{i\hat{h}(r)}}. \tag{5.59}$$

where $\hat{h} = \int h(r) dr$, which in fact in the form of the cylindrical imploding wave. Asymptotic solutions are again harmonic solutions but with different speed of sound values. Near the event horizon and at $r \to +\infty$, the solution of Eq.5.45 reduces asymptotically to harmonic solutions

$$H(r_*) = e^{-i\frac{\omega}{c_\infty} r_*} + \mathcal{R} e^{+i\frac{\omega}{c_\infty} r_*}, r^* \to +\infty \tag{5.60}$$

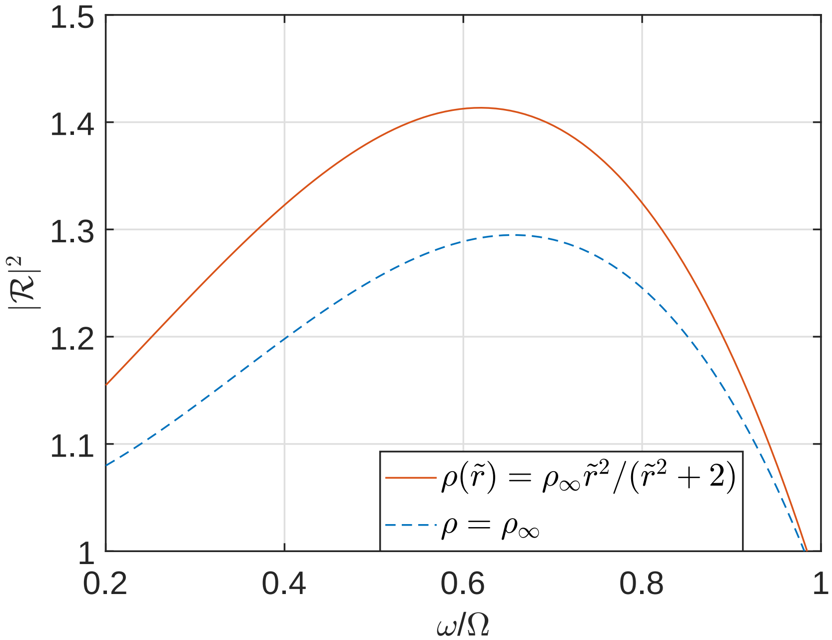

Figure 5.18: $|R|^2$ is calculated for superradiant case with $\tilde{\Omega} = \sqrt{2}$ in constant and non-constant density profiles.

$$H(r_*) = \mathcal{T} e^{-\frac{i}{c(r_h)}\left(\omega - \frac{m v_{\hat{\phi}}(r_h)}{r_h}\right) r^*}, r^* \to -\infty. \tag{5.61}$$

The Wronskian for the solutions with its complex conjugate yields the relation between the reflection and transmission coefficients as,

$$1 - |\mathcal{R}|^2 = \sqrt{3}\left(\frac{\omega - m\Omega}{\omega}\right)\left|\mathcal{T}^2\right|, \tag{5.62}$$

which gives the superradiant $\left(|\mathcal{R}|^2\right) > 1$ condition as $\omega < m\Omega$. In order to calculate the reflection coefficient with respect to ω for different rotational frequencies, we solved the Eq.5.43 and Eq.5.45 together and analyze the Fourier components of the asymptotic far field solutions. Fig.5.18 shows the comparison between the previous assumption, constant density, and the new density profile. The differences in the reflection coefficients is higher between $0.4 < \omega/\Omega < 0.7$ and peaks at $\omega/\Omega = 0.52$, shows that new density profile resulted nearly %9 increase with respect to constant density profile, while in the $\omega/\Omega \cong 1$ limit they both take the value of one.

Chapter 6

CONCLUSION

This thesis investigated the acoustic superradiance from the vortex state in an unbound Bose-Einstein condensate, which manifests itself as the amplified scattering of coaxial acoustic perturbations from the vortex. The study provides solid contributions through (1) a qualitative assessment of the constant background density approximation that is commonly employed in the literature, by comparing its results to that of a radially varying density profile, that is obtained self-consistently through the solution of the Gross-Pitaevskii equation for the BEC-vortex state; (2) quantitative and performance comparison of the time-domain and asymptotic frequency domain calculations of the superradiance.

The first outcome is that the self-consistent density profile renders the curved-space time landscape of the analogue black-hole and the propagation dynamics substantially different than that of the constant-density approximation since density-dependent physical parameters (e.g. sound propagation speed) become inherently a function of position (radial coordinate) and all black-hole landmarks (event horizon, ergoregion) are relocated accordingly. A significant outcome is that the use of the self-consistent density profile improves on the transient behavior of the scattering process within the ergoregion by eliminating the overshoot behavior of the perturbative wave's energy, while providing a slightly higher amplification of the wave. Numerical calculations show that for perturbative waves with low-frequency (compared to the vortex angular frequency), the two density models differ significantly in the magnitude of superradiance. This difference disappears at the high-frequency regime of the waves.

The second contribution demonstrates the impact of the mathematical formulation and its numerical implementation. Time domain calculations have the potential to give insight about the transient behavior of the perturbative wave within the ergoregion during the interaction with the event horizon. It is already known that the time-domain simulation faces numerical challenges near the horizon and beyond where no specific physical boundary condition is applicable. We employ a number of techniques to suppress the numerical instabilities arising in this region through physical constraints imposed at the event horizon. Fortunately, integrated quantities (like energy) can be obtained smoothly. On the other hand, the asymptotic frequency domain calculations apply a far-field analysis by mapping the event horizon to -infinity through the so-called Tortoise coordinate transformation. Consequently, the far-field form of the wave can be investigated through its Fourier components with no numerical instabilities as the coordinate singularity of the event horizon is eliminated. This gives a fast and efficient way of obtaining the reflection coefficient of the asymptotic form of the perturbative wave and hence the computation of superradiance.

Evidently, the thesis work can provide a basis for future studies in which the model can be improved and extended. For improvement, one can introduce a sink to the vortex to better account for the draining-bathtub model. The formulation can be applied in a straightforward manner to vortices with higher winding numbers where the density profile for each winding number has to be obtained self-consistently. Provided that these vortices are stable, it may give different superradiance profiles. Finally, one can introduce confinement potentials through the Gross-Pitaevskii equation which may have profound impact on the dynamics of the superradiance.

Appendix A

DERIVATION OF NULL VECTORS

The Lagrangian for the line equation 3.66 can be written as

$$2\mathcal{L} = \left(\upsilon^2 - c^2\right)\dot{t}^2 + \frac{c^2}{c^2 - \upsilon_r^2}\dot{r}^2 + r^2\dot{\theta}^2 - 2\upsilon_\theta r\dot{\theta}\dot{t}, \tag{A.1}$$

here, dots represent the derivative with respect to proper time, τ. Only two quantity is conserved, the energy of the phonon, E and the angular momentum, L and for the null geodesics we have

$$-E\dot{t} + L\dot{\theta} + \frac{c^2}{c^2 - \upsilon_r^2}\dot{r}^2 = 0. \tag{A.2}$$

Conserved quantities are

$$p_t = \frac{\partial\mathcal{L}}{\partial\dot{t}} = \left(\upsilon^2 - c^2\right)\dot{t} - r\upsilon_\theta\dot{\theta} = -E, \tag{A.3}$$

$$p_\theta = \frac{\partial\mathcal{L}}{\partial\dot{\theta}} = -r\upsilon_\theta\dot{t} + r^2\dot{\theta} = L \tag{A.4}$$

which in turns gives

$$\dot{t} = \frac{1}{r\upsilon_\theta}\left(r^2\dot{\theta} - L\right), \tag{A.5}$$

$$E = \frac{\upsilon^2 - c^2}{r\upsilon_\theta}\left(L - r^2\dot{\theta}\right) + r\upsilon_\theta\dot{\theta}, \tag{A.6}$$

$$\dot{\theta} = \frac{-E\upsilon_\theta r + \left(\upsilon^2 - c^2\right) L}{r^2 \left(\upsilon_r^2 - c^2\right)}. \tag{A.7}$$

From Eq.A.5 we hahe

$$\dot{t} = \frac{Er - L\upsilon_\theta}{r\left(c^2 - \upsilon_r^2\right)}, \tag{A.8}$$

and finally inserting $\dot{\theta}$ and $\dot{t}$ into the Eq.A.2 give $\dot{r}$ as

$$\dot{r}^2 = \frac{E^2}{c^2} - \frac{2EL\upsilon_\theta}{rc^2} + \frac{L^2}{r^2c^2}\left(\upsilon^2 - c^2\right). \tag{A.9}$$

Considering at $r \to \infty$ motion is purely radial, zero angular momentum is the approximation we will consider in order to set the boundaries, which gives the geodesics as,

$$\dot{r} = \pm\frac{E}{c}, \tag{A.10}$$

$$\dot{\theta} = \frac{-E\upsilon_\theta r}{r^2\left(\upsilon_r^2 - c^2\right)}, \tag{A.11}$$

$$\dot{t} = -\frac{E}{\upsilon_r^2 - c^2}. \tag{A.12}$$

The total angular momentum can be written using the Eq. A.7

$$L' = r^2\dot{\theta} = -\frac{E\upsilon_\theta r}{\upsilon_r^2 - c^2} + L\frac{\upsilon^2 - c^2}{\upsilon_r^2 - c^2}, \tag{A.13}$$

and at infinity, it consists of fluid angular momentum and the phonon angular momentum due to frame dragging effect,

$$L' = L + \frac{E\upsilon_\theta r}{c^2}. \tag{A.14}$$

Associated four velocity vectors for the incoming and the outgoing waves can be written from the geodesics with the coefficients from A.2,

$$U^{\mu}_{in} = \left[\frac{E}{c\,(c-\upsilon_r)}, -\frac{E}{c}, \frac{E\upsilon_\theta}{c\,(c-\upsilon_r)}\right], \tag{A.15}$$

$$U^{\mu}_{out} = \left[\frac{E}{c\,(\upsilon_r+c)}, \frac{E}{c}, \frac{E\upsilon_\theta}{c\,(\upsilon_r+c)}\right]. \tag{A.16}$$

Finally we can set up directional derivatives to the wave equation as

$$U^{\mu}_{in}\partial_\mu\Phi_1 = \frac{E}{c\,(c-\upsilon_r)}\partial_t\Phi_1 - \frac{E}{c}\partial_r\Phi_1 + \frac{E\upsilon_\theta}{c\,(c-\upsilon_r)}\partial_\theta\Phi_1 \tag{A.17}$$
$$=\frac{E}{c\,(c-\upsilon_r)}\left(-c\Pi - \upsilon_r\Gamma - \frac{im\upsilon_\theta}{r}\Phi_1\right) - \frac{E}{c}\Gamma + \frac{E\upsilon_\theta}{c\,(c-\upsilon_r)}im\Phi_1 \tag{A.18}$$
$$\frac{E}{c\,(c-\upsilon_r)}\left(\Pi+\Gamma\right), \tag{A.19}$$

$$U^{\mu}_{out}\partial_\mu\Phi_1 = \frac{E}{c\,(c+\upsilon_r)}\partial_t\Phi_1 + \frac{E}{c}\partial_r\Phi_1 + \frac{E\upsilon_\theta}{c\,(c+\upsilon_r)}\partial_\theta\Phi_1 \tag{A.20}$$
$$=\frac{E}{c\,(c+\upsilon_r)}\left(-c\Pi - \upsilon_r\Gamma - \frac{im\upsilon_\theta}{r}\Phi_1\right) + \frac{E}{c}\Gamma + \frac{E\upsilon_\theta}{c\,(c+\upsilon_r)}im\Phi_1 \tag{A.21}$$
$$\frac{E}{c\,(c+\upsilon_r)}\left(\Gamma-\Pi\right). \tag{A.22}$$

Appendix B

KLEIN-GORDON EQUATION

The explicit form of the KG equation,

$$\begin{aligned}&\left[\frac{\partial^2}{\partial t^2}+2\upsilon_r\frac{\partial^2}{\partial t\partial r}+\frac{2\upsilon_\theta}{r}\frac{\partial^2}{\partial t\partial\theta}+\left(-c^2+\upsilon_r^2\right)\frac{\partial^2}{\partial r^2}+\frac{2\upsilon_\theta\upsilon_r}{r}\frac{\partial^2}{\partial r\partial\theta}\right.\\&+\left(-\frac{c^2}{r^2}+\frac{\upsilon_\theta^2}{r^2}\right)\frac{\partial^2}{\partial\theta^2}+\frac{1}{r}\frac{\partial(r\upsilon_r)}{\partial r}\frac{\partial}{\partial t}+\left(-\frac{\upsilon_\theta\upsilon_r}{r^2}+\frac{\upsilon_\theta}{r}\frac{\partial\upsilon_r}{\partial r}\right)\frac{\partial}{\partial\theta}\\&\left.+\left(-\frac{c^2}{r}-\frac{c^2}{\rho}\frac{\partial\rho(r)}{\partial r}+\frac{\upsilon^2}{r}+2\upsilon_r\frac{\partial\upsilon_r}{\partial r}+\upsilon_\theta\frac{\partial\upsilon_\theta}{\partial r}\right)\frac{\partial}{\partial r}-c^2\frac{\partial^2}{\partial z^2}\right]\Phi_1=0,\end{aligned}\tag{B.1}$$

with a formal solution of the form,

$$\Phi_1=P(r)e^{i(m\theta-\omega t)}\tag{B.2}$$

is written as

$$\partial_r^2P(r)+Q(r)\partial_rP(r)+Z(r)P(r)=0,\tag{B.3}$$

$$Q(r)=\left(-2i\omega\upsilon_r+\frac{2im\upsilon_r\upsilon_\theta}{r}-\frac{\upsilon_\theta^2+\upsilon_r^2-c^2}{r}-\frac{c^2}{\rho}\partial_r\rho+\partial_r\left(\upsilon_r^2+\frac{\upsilon_\theta^2}{2}\right)\right)\frac{1}{\upsilon_r^2-c^2},\tag{B.4}$$

$$Z(r)=\left(-\omega^2+\frac{2m\omega\upsilon_\theta}{r}-m^2\frac{\upsilon_\theta^2-c^2}{r^2}-\frac{i\omega\partial_r(r\upsilon_r)}{r}-\frac{im\upsilon_\theta\upsilon_r}{r^2}+\frac{im\upsilon_\theta\partial_r\upsilon_r}{r}\right)\frac{1}{\upsilon_r^2-c^2}.\tag{B.5}$$

The tortoise coordinate

$$\Delta=\frac{dr_*}{dr}=\left(1-\frac{\upsilon_r^2}{c^2}\right)^{-1}\tag{B.6}$$

helps to express the radial part of the Eq.B.2 by the product of two functions, $P(r) = H(r_*)R(r)$. Introducing $P(r)$ into equation above gives,

$$\partial_r^2 (H(r_*)R(r)) + Q(r)\partial_r (H(r_*)R(r)) + Z(r)H(r_*)R(r) = \tag{B.7}$$

$$=\partial_r (H(r_*)\partial_r R(r) + \partial_r r_* \partial_{r_*} H(r_*) R(r)) + Q(r) (H(r_*)\partial_r R(r) + \partial_r r_* \partial_{r_*} H(r_*) R(r))$$
$$+ Z(r)H(r_*)R(r) = \tag{B.8}$$

$$=H(r_*)\partial_r^2 R(r) + 2\Delta\partial_{r_*} H(r_*)\partial_r R(r) + R(r)\partial_r \Delta\partial_{r_*} H(r_*) + R(r)\Delta^2\partial_{r_*}^2 H(r_*)$$
$$+ Q(r) H(r_*)\partial_r R(r) + \Delta Q(r) R(r)\partial_{r_*} H(r_*) + Z(r)H(r_*)R(r) = \tag{B.9}$$

$$=R(r)\Delta^2\partial_{r_*}^2 H(r_*) + \partial_{r_*} H(r_*) (2\Delta\partial_r R(r) + R(r)\partial_r \Delta + \Delta Q(r) R(r))$$
$$+ H(r_*) \left(\partial_r^2 R(r) + Q(r)\partial_r R(r) + Z(r) R(r)\right). \tag{B.10}$$

In order to preserve the Schrodinger like form of the wave equation the coefficient of the $\partial_{r_*} H(r_*)$ has to be null, which gives two main equations to be solved. The first equation is for the function $R(r)$

$$\partial_r R(r) + R(r)\frac{(\partial_r \Delta + \Delta Q(r))}{2\Delta} = 0, \tag{B.11}$$

$$M(r) = \frac{(\partial_r \Delta + \Delta Q(r))}{2\Delta} = \tag{B.12}$$

$$= \frac{(6\xi^2 + r^2)}{2r(2\xi^2 + r^2)} - i\frac{\upsilon_r (m\upsilon_\theta - \omega r)}{r(\upsilon_r^2 - c^2)}, \tag{B.13}$$

$$R(r) = C exp\left(-\int M(r)dr\right) \tag{B.14}$$

$$= C\left(\frac{r^2 + 2\xi^2}{r^3}\right)^{1/2} exp\left(-i\int \frac{\upsilon_r (m\upsilon_\theta - \omega r)}{r(\upsilon_r^2 - c^2)}dr\right), \tag{B.15}$$

where C is an arbitrary constant. The second equation is for $H\left(r_*\right)$,

$$\partial_{r_*}^2 H\left(r_*\right) + \frac{H\left(r_*\right)}{\Delta^2}\left(\frac{\partial_r^2 R\left(r\right)}{R\left(r\right)} + Q\left(r\right)\frac{\partial_r R(r)}{R\left(r\right)} + Z\left(r\right)\right) = 0, \tag{B.16}$$

$$\partial_{r_*}^2 H\left(r_*\right) + \frac{H\left(r_*\right)}{\Delta^2}\left(\partial_r\left(\frac{\partial_r R\left(r\right)}{R\left(r\right)}\right) + \left(\frac{\partial_r R\left(r\right)}{R\left(r\right)}\right)^2 + Q\left(r\right)\frac{\partial_r R(r)}{R\left(r\right)} + Z\left(r\right)\right) = 0, \tag{B.17}$$

$$\partial_{r_*}^2 H\left(r_*\right) + \frac{H\left(r_*\right)}{\Delta^2}\left(-\partial_r M + M^2 - Q\left(r\right)M + Z\left(r\right)\right) = 0 \tag{B.18}$$

$$V\left(r\right) = \frac{-\partial_r M + M^2 - Q\left(r\right)M + Z\left(r\right)}{\Delta^2}, \tag{B.19}$$

$$= \left(\frac{\omega}{c} - \frac{m\upsilon_\theta}{rc}\right)^2 + \frac{\left(\upsilon_r^2 - c^2\right)\upsilon_r^2\left(5r^4 + 76r^2\xi^2 + 180\xi^4\right)}{4c^4r^2(r^2+2\xi^2)^2}$$
$$+ \frac{\left(\upsilon_r^2 - c^2\right)\left(4m^2\left(r^2+2\xi^2\right)^2 - r^4 - 20r^2\xi^2 + 12\xi^4\right)}{4c^2r^2\left(r^2+2\xi^2\right)^2}. \tag{B.20}$$

Finally wave equation B.2 becomes,

$$\Phi_1 = P(r)e^{i(m\theta-\omega t)}, \tag{B.21}$$

$$= H\left(r_*\right)R\left(r\right)e^{i(m\theta-\omega t)} \tag{B.22}$$

$$= H\left(r_*\right)\left(\frac{r^2+2\xi^2}{r^3}\right)^{1/2} e^{i(m\theta-\omega t)}e^{-i\int h(r)dr}, \tag{B.23}$$

$$h\left(r\right) = \frac{\upsilon_r\left(m\upsilon_\theta - \omega r\right)}{r\left(\upsilon_r^2 - c^2\right)}e^{i(m\theta-\omega t)}. \tag{B.24}$$

Appendix C

DERIVATION OF THE CONJUGATE FIELDS

The line element is

$$ds^2 = -\alpha^2 dt^2 + \gamma_{ij}(dx^i + \beta^i dt)(dx^j + \beta^j dt), \tag{C.1}$$

where $\alpha = c$, $\gamma_{ij} = diag(1, r^2, 1)$ and $\beta^i = (-\upsilon_r, -\upsilon_\theta/r, 0)$. Two conjugate fields are introduced accordingly:

$$\Gamma_i = \frac{\partial \Phi_1}{\partial x^i} \qquad \Pi = -\frac{1}{c}\left(\frac{\partial \Phi_1}{\partial t} - \beta^i \Gamma_i\right), \tag{C.2}$$

where $x_i = (r, \theta, z)$ and $\beta^i = (-\upsilon_r, -\upsilon_\theta/r, 0)$. The fields are introduced formally as

$$\Phi_1 = \phi_1(t,r)e^{im\theta}e^{ikz} \qquad \Pi = \pi_1(t,r)e^{im\theta}e^{ikz} \qquad \Gamma_1 = \gamma_1(t,r)e^{im\theta}e^{ikz} \tag{C.3}$$

with (k, m) denoting the axial and azimuthal wave numbers and Γ_i is calculated as

$$\Gamma_i = [\gamma_1 \;\; im\phi_1 \;\; ik\phi_1]e^{im\theta}e^{ikz}. \tag{C.4}$$

Definition of the field Π gives the first equation for the term $\partial_t \phi_1$ as,

$$\Pi = -1/c\left(\partial_t \Phi_1 - \beta^i \Gamma_i\right), \tag{C.5}$$

$$\partial_t \Phi_1 = -c\Pi + \beta^1 \Gamma_1 + \beta^2 \Gamma_2, \tag{C.6}$$

$$\partial_t \phi_1 = -c\pi - \upsilon_r \gamma_1 - im\upsilon_\theta \phi_1/r. \tag{C.7}$$

For the second equation, $\partial_r(\partial_t\phi_1)$ provides the equation of $\partial_t\gamma_1$ as,

$$\Gamma_i = \partial_{x^i}\Phi_1, \tag{C.8}$$

$$\partial_t\Gamma_1 = \partial_t\partial_r\Phi_1, \tag{C.9}$$

$$\partial_t\gamma_1 = \partial_r(\partial_t\phi_1) = \partial_r(-c\pi - \upsilon_r\gamma_1 - im\upsilon_\theta\phi_1/r) \tag{C.10}$$

$$= -c\partial_r\pi - \pi\partial_r c - \upsilon_r\partial_r\gamma_1 - \gamma_1\partial_r\upsilon_r - im\phi_1\partial_r\upsilon_\theta/r + im\phi_1\upsilon_\theta/r^2 - im\upsilon_\theta\partial_r\phi_1/r. \tag{C.11}$$

Now we have the first two, we need to implement both to the KG equation 5.2,

$$\partial_t^2\phi_1 + 2\upsilon_r\partial_t\gamma_1 + 2im\upsilon_\theta\partial_t\phi_1/r + \left(-c^2+\upsilon_r^2\right)\partial_r\gamma_1 + 2im\upsilon_\theta\partial_r\phi_1/r$$
$$+\left(m^2c^2/r^2 - m^2\upsilon_\theta^2/r^2\right)\phi_1 + (\upsilon_r + \partial_r\upsilon_r/r)\partial_t\phi_1 + \left(-im\upsilon_\theta\upsilon_r/r^2 + im\upsilon_\theta\partial_r\upsilon_r/r\right)\phi_1$$
$$+\left(-c^2/r - c^2\partial_r\rho/\rho + \upsilon^2/r + 2\upsilon_r\partial_r\upsilon_r + \upsilon_\theta\partial_r\upsilon_\theta\right)\partial_r\phi_1 + c^2k^2\phi_1 = 0 \tag{C.12}$$

and in order to that we have to calculate

$$\partial_t^2\Phi_1 = \partial_t(-c\pi - \upsilon_r\gamma_1 - im\upsilon_\theta\phi_1/r)\,e^{im\theta}e^{ikz} \tag{C.13}$$

$$= (-c\partial_t\pi - \upsilon_r\partial_t\gamma_1 - im\upsilon_\theta\partial_t\phi_1/r)\,e^{im\theta}e^{ikz} \tag{C.14}$$

$$= \left(-c\partial_t\pi + \upsilon_r c\partial_r\pi + \upsilon_r\pi\partial_r c + \upsilon_r^2\partial_r\gamma_1 + \upsilon_r\gamma_1\partial_r\upsilon_r + im\upsilon_r\phi_1\partial_r\upsilon_\theta/r\right.$$
$$\left.-im\upsilon_r\phi_1\upsilon_\theta/r^2 + im\upsilon_\theta\upsilon_r\partial_r\phi_1/r + im\upsilon_\theta c\pi/r + im\upsilon_\theta\upsilon_r\gamma_1/r - m^2\upsilon_\theta^2\phi_1/r^2\right)e^{im\theta}e^{ikz}. \tag{C.15}$$

Now, inserting $\partial_t^2\phi_1$ and the time derivatives; $\partial_t\gamma_1$ and $\partial_t\phi_1$ into equation above we reach the final time derivative we need,

$$\partial_t\pi_1 = \pi_1(-\upsilon_r\partial_r c/c - im\upsilon_\theta/r - \partial_r(r\upsilon_r)/r) - \upsilon_r\partial_r\pi_1 - c\partial_r\gamma_1$$
$$+\gamma_1\left(-c/r - c/\rho\partial_r\rho + \upsilon_\theta^2/rc + \upsilon_\theta\partial_r\upsilon_\theta/c\right) + \phi_1\left(m^2c/r^2 + ck^2 - im\upsilon_r\partial_r\upsilon_\theta/rc - im\upsilon_r\upsilon_\theta/r^2\right). \tag{C.16}$$

BIBLIOGRAPHY

[1] Robert M Wald. *General relativity.* Chicago Univ. Press, Chicago, IL, 1984.

[2] Remo Ruffini and John A Wheeler. Introducing the black hole. *Physics Today*, 1971.

[3] Frank Watson Dyson, Arthur Stanley Eddington, and Charles Davidson. Ix. a determination of the deflection of light by the sun's gravitational field, from observations made at the total eclipse of may 29, 1919. *Philosophical Transactions of the Royal Society of London. Series A, Containing Papers of a Mathematical or Physical Character*, 220(571-581):291–333, 1920.

[4] K Schwarzschild. Sitzungsber. dtsch. akad. wiss. berlin, kl. math. *Phys. Tech*, 189:1916, 1916.

[5] Roy P Kerr. Gravitational field of a spinning mass as an example of algebraically special metrics. *Physical review letters*, 11(5):237, 1963.

[6] Benjamin P Abbott, Richard Abbott, TD Abbott, MR Abernathy, Fausto Acernese, Kendall Ackley, Carl Adams, Thomas Adams, Paolo Addesso, RX Adhikari, et al. Observation of gravitational waves from a binary black hole merger. *Physical review letters*, 116(6):061102, 2016.

[7] BP Abbott, R Abbott, TD Abbott, S Abraham, F Acernese, K Ackley, C Adams, RX Adhikari, VB Adya, C Affeldt, et al. Searches for continuous gravitational waves from 15 supernova remnants and fomalhaut b with advanced ligo. *The Astrophysical Journal*, 875(2):122, 2019.

[8] Kazunori Akiyama, Antxon Alberdi, Walter Alef, Keiichi Asada, Rebecca Azulay, Anne-Kathrin Baczko, David Ball, Mislav Baloković, John Barrett, Dan Bintley, et al. First m87 event horizon telescope results. i. the shadow of the supermassive black hole. *The Astrophysical Journal Letters*, 875(1):L1, 2019.

[9] Roger Penrose. Gravitational collapse: The role of general relativity (reprinted from rivista del nuovo cimento, numero speziale, i, vol 257, 1969). *General Relativity and Gravitation*, 34(7):1141–1165, 2002.

[10] Ya B Zel'Dovich. Generation of waves by a rotating body. *ZhETF Pisma Redaktsiiu*, 14:270, 1971.

[11] Stephen W Hawking. Black hole explosions? *Nature*, 248(5443):30, 1974.

[12] Stephen W Hawking. Particle creation by black holes. *Communications in mathematical physics*, 43(3):199–220, 1975.

[13] Jacob D Bekenstein. Black holes and entropy. *Physical Review D*, 7(8):2333, 1973.

[14] Matt Visser. Acoustic black holes: horizons, ergospheres and hawking radiation. *Classical and Quantum Gravity*, 15(6):1767, 1998.

[15] Silke Christine Edith Weinfurtner. *Emergent Spacetimes: A Thesis Submitted to the Victoria University of Wellington in Fulfilment of the Requirements for the Degree of Doctor of Philosophy in Mathematics*. PhD thesis, Victoria University of Wellington, 2007.

[16] Richard W White. Acoustic ray tracing in moving inhomogeneous fluids. *The Journal of the Acoustical Society of America*, 53(6):1700–1704, 1973.

[17] W. G. Unruh. Experimental black-hole evaporation? *Phys. Rev. Lett.*, 46:1351–1353, May 1981.

[18] Theodore Jacobson. Black-hole evaporation and ultrashort distances. *Physical Review D*, 44(6):1731, 1991.

[19] TA Jacobson and GE Volovik. Event horizons and ergoregions in 3 he. *Physical Review D*, 58(6):064021, 1998.

[20] GE Volovik. Is there analogy between quantized vortex and black hole? *arXiv preprint gr-qc/9510001*, 1995.

[21] S Giovanazzi. Hawking radiation in sonic black holes. *Physical review letters*, 94(6):061302, 2005.

[22] Alessio Recati, Nicolas Pavloff, and Iacopo Carusotto. Bogoliubov theory of acoustic hawking radiation in bose-einstein condensates. *Physical Review A*, 80(4):043603, 2009.

[23] William G Unruh and Ralf Schützhold. Universality of the hawking effect. *Physical Review D*, 71(2):024028, 2005.

[24] Carlos Barcelo, Stefano Liberati, Sebastiano Sonego, and Matt Visser. Hawking-like radiation does not require a trapped region. *Physical review letters*, 97(17):171301, 2006.

[25] Luis Javier Garay, JR Anglin, J Ignacio Cirac, and P Zoller. Sonic black holes in dilute bose-einstein condensates. *Physical Review A*, 63(2):023611, 2001.

[26] Luis Javier Garay, JR Anglin, J Ignacio Cirac, and P Zoller. Sonic analog of gravitational black holes in bose-einstein condensates. *Physical Review Letters*, 85(22):4643, 2000.

[27] Carlos Barcelo, Stefano Liberati, and Matt Visser. Probing semiclassical analog gravity in bose-einstein condensates with widely tunable interactions. *Physical Review A*, 68(5):053613, 2003.

[28] Piyush Jain, Silke Weinfurtner, Matt Visser, and CW Gardiner. Analog model of a friedmann-robertson-walker universe in bose-einstein condensates: Application of the classical field method. *Physical Review A*, 76(3):033616, 2007.

[29] Petr O Fedichev and Uwe R Fischer. Gibbons-hawking effect in the sonic de sitter space-time of an expanding bose-einstein-condensed gas. *Physical review letters*, 91(24):240407, 2003.

[30] Nader Ghazanfari and Özgür Esat Müstecaplıoğlu. Acoustic superradiance from an optical-superradiance-induced vortex in a bose-einstein condensate. *Physical Review A*, 89(4):043619, 2014.

[31] B Reznik. Origin of the thermal radiation in a solid-state analogue of a black hole. *Physical Review D*, 62(4):044044, 2000.

[32] B Reznik. Trans-planckian tail in a theory with a cutoff. *Physical Review D*, 55(4):2152, 1997.

[33] David Vocke, Calum Maitland, Angus Prain, Kali E Wilson, Fabio Biancalana, Ewan M Wright, Francesco Marino, and Daniele Faccio. Rotating black hole geometries in a two-dimensional photon superfluid. *Optica*, 5(9):1099–1103, 2018.

[34] M. Elazar, V. Fleurov, and S. Bar-Ad. All-optical event horizon in an optical analog of a laval nozzle. *Phys. Rev. A*, 86:063821, Dec 2012.

[35] Thomas G Philbin, Chris Kuklewicz, Scott Robertson, Stephen Hill, Friedrich König, and Ulf Leonhardt. Fiber-optical analog of the event horizon. *Science*, 319(5868):1367–1370, 2008.

[36] Luca Giacomelli and Stefano Liberati. Rotating black hole solutions in relativistic analogue gravity. *arXiv preprint arXiv:1705.05696*, 2017.

[37] Peter VE McClintock. The universe in a helium droplet. *Contemporary Physics*, 45(2):187–188, 2004.

[38] GE Volovik. Simulation of quantum field theory and gravity in superfluid 3 he. *Low Temperature Physics*, 24(2):127–129, 1998.

[39] Maurício Richartz, Angus Prain, Stefano Liberati, and Silke Weinfurtner. Rotating black holes in a draining bathtub: superradiant scattering of gravity waves. *Physical Review D*, 91(12):124018, 2015.

[40] Ralf Schützhold and William G Unruh. Gravity wave analogues of black holes. *Physical Review D*, 66(4):044019, 2002.

[41] Germain Rousseaux, Christian Mathis, Philippe Maïssa, Thomas G Philbin, and Ulf Leonhardt. Observation of negative-frequency waves in a water tank: a classical analogue to the hawking effect? *New Journal of Physics*, 10(5):053015, 2008.

[42] Carlos Barceló, Stefano Liberati, and Matt Visser. Analogue gravity. *Living reviews in relativity*, 14(1):3, 2011.

[43] Silke Weinfurtner, Edmund W. Tedford, Matthew C. J. Penrice, William G. Unruh, and Gregory A. Lawrence. Measurement of stimulated hawking emission in an analogue system. *Phys. Rev. Lett.*, 106:021302, Jan 2011.

[44] Oren Lahav, Amir Itah, Alex Blumkin, Carmit Gordon, Shahar Rinott, Alona Zayats, and Jeff Steinhauer. Realization of a sonic black hole analog in a bose-einstein condensate. *Phys. Rev. Lett.*, 105:240401, Dec 2010.

[45] Theo Torres, Sam Patrick, Antonin Coutant, Mauricio Richartz, Edmund W Tedford, and Silke Weinfurtner. Rotational superradiant scattering in a vortex flow. *Nature Physics*, 13(9):833, 2017.

[46] Jeff Steinhauer. Observation of self-amplifying hawking radiation in an analogue black-hole laser. *Nature Physics*, 10(11):864, 2014.

[47] Jeff Steinhauer. Observation of quantum hawking radiation and its entanglement in an analogue black hole. *Nature Physics*, 12(10):959, 2016.

[48] William Unruh and Ralf Schützhold. *Quantum analogues: from phase transitions to black holes and cosmology*, volume 718. Springer, 2007.

[49] Soumen Basak and Parthasarathi Majumdar. Reflection coefficient for superresonant scattering. *Classical and Quantum Gravity*, 20(13):2929, 2003.

[50] R Balbinot, A Fabbri, S Fagnocchi, and R Parentani. Hawking radiation from acoustic black holes, short distance and back-reaction effects. *arXiv preprint gr-qc/0601079*, 2006.

[51] Silke Weinfurtner, Edmund W Tedford, Matthew CJ Penrice, William G Unruh, and Gregory A Lawrence. Classical aspects of hawking radiation verified in analogue gravity experiment. In *Analogue Gravity Phenomenology*, pages 167–180. Springer, 2013.

[52] Léo-Paul Euvé, Scott Robertson, Nicolas James, Alessandro Fabbri, and Germain Rousseaux. Scattering of surface waves on an analogue black hole. *arXiv preprint arXiv:1806.05539*, 2018.

[53] Florent Michel and Renaud Parentani. Probing the thermal character of analogue hawking radiation for shallow water waves? *Physical Review D*, 90(4):044033, 2014.

[54] Antonin Coutant and Silke Weinfurtner. The imprint of the analogue hawking effect in subcritical flows. *Physical Review D*, 94(6):064026, 2016.

[55] Vitor Cardoso, Antonin Coutant, Mauricio Richartz, and Silke Weinfurtner. Detecting rotational superradiance in fluid laboratories. *Phys. Rev. Lett.*, 117:271101, Dec 2016.

[56] Carlos Barceló, Stefano Liberati, and Matt Visser. Refringence, field theory and normal modes. *Classical and Quantum Gravity*, 19(11):2961, 2002.

[57] Petr O Fedichev and Uwe R Fischer. Observer dependence for the phonon content of the sound field living on the effective curved space-time background of a bose-einstein condensate. *Physical Review D*, 69(6):064021, 2004.

[58] L-P Euvé, Florent Michel, Renaud Parentani, Thomas G Philbin, and Germain Rousseaux. Observation of noise correlated by the hawking effect in a water tank. *Physical review letters*, 117(12):121301, 2016.

[59] Iacopo Carusotto, Serena Fagnocchi, Alessio Recati, Roberto Balbinot, and Alessandro Fabbri. Numerical observation of hawking radiation from acoustic black holes in atomic bose–einstein condensates. *New Journal of Physics*, 10(10):103001, 2008.

[60] Stefano Finazzi and Renaud Parentani. Spectral properties of acoustic black hole radiation: broadening the horizon. *Physical Review D*, 83(8):084010, 2011.

[61] U Leonhardt, T Kiss, and P Öhberg. Theory of elementary excitations in unstable bose-einstein condensates and the instability of sonic horizons. *Physical Review A*, 67(3):033602, 2003.

[62] Carlos Mayoral, Alessio Recati, Alessandro Fabbri, Renaud Parentani, Roberto Balbinot, and Iacopo Carusotto. Acoustic white holes in flowing atomic bose–einstein condensates. *New Journal of Physics*, 13(2):025007, 2011.

[63] Germain Rousseaux and Yury Stepanyants. Modeling of bose–einstein condensation in a water tank. In *Nonlinear Waves and Pattern Dynamics*, pages 91–101. Springer, 2018.

[64] M Tettamanti, SL Cacciatori, A Parola, and I Carusotto. Numerical study of a recent black-hole lasing experiment. *EPL (Europhysics Letters)*, 114(6):60011, 2016.

[65] Yi-Hsieh Wang, Ted Jacobson, Mark Edwards, and Charles W Clark. Mechanism of stimulated hawking radiation in a laboratory bose-einstein condensate. *Physical Review A*, 96(2):023616, 2017.

[66] Andreas Finke, Piyush Jain, and Silke Weinfurtner. On the observation of nonclassical excitations in bose–einstein condensates. *New Journal of Physics*, 18(11):113017, 2016.

[67] Ulf Leonhardt. Questioning the recent observation of quantum hawking radiation. *Annalen der Physik*, 530(5):1700114, 2018.

[68] Jeff Steinhauer. Response to version 2 of the note concerning the observation of quantum hawking radiation and its entanglement in an analogue black hole. *arXiv preprint arXiv:1609.09017*, 2016.

[69] Florent Michel, Jean-François Coupechoux, and Renaud Parentani. Phonon spectrum and correlations in a transonic flow of an atomic bose gas. *Physical Review D*, 94(8):084027, 2016.

[70] James E Lidsey. Cosmic dynamics of bose–einstein condensates. *Classical and Quantum Gravity*, 21(4):777, 2004.

[71] Esteban Adolfo Calzetta and BL Hu. Bose-einstein condensate collapse and dynamical squeezing of vacuum fluctuations. *Physical Review A*, 68(4):043625, 2003.

[72] Silke Weinfurtner, Stefano Liberati, and Matt Visser. Analogue model for quantum gravity phenomenology. *Journal of Physics A: Mathematical and General*, 39(21):6807, 2006.

[73] Florian Girelli, Stefano Liberati, and Lorenzo Sindoni. Gravitational dynamics in bose-einstein condensates. *Physical Review D*, 78(8):084013, 2008.

[74] Stefano Finazzi, Stefano Liberati, and Lorenzo Sindoni. Cosmological constant: A lesson from bose-einstein condensates. *Physical review letters*, 108(7):071101, 2012.

[75] Florian Kühnel and Cornelius Rampf. Astrophysical bose-einstein condensates and superradiance. *Physical Review D*, 90(10):103526, 2014.

[76] Bose. Plancks gesetz und lichtquantenhypothese. *Zeitschrift für Physik*, 26(1):178–181, Dec 1924.

[77] Albert Einstein. Quantentheorie des einatomigen idealen gases. *SB Preuss. Akad. Wiss. phys.-math. Klasse*, 1924.

[78] Wolfgang Ketterle, Dallin S Durfee, and DM Stamper-Kurn. Making, probing and understanding bose-einstein condensates. *arXiv preprint cond-mat/9904034*, 1999.

[79] Mike H Anderson, Jason R Ensher, Michael R Matthews, Carl E Wieman, and Eric A Cornell. Observation of bose-einstein condensation in a dilute atomic vapor. *science*, 269(5221):198–201, 1995.

[80] Kendall B Davis, M-O Mewes, Michael R Andrews, NJ Van Druten, DS Durfee, DM Kurn, and Wolfgang Ketterle. Bose-einstein condensation in a gas of sodium atoms. *Physical review letters*, 75(22):3969, 1995.

[81] Cl C Bradley, CA Sackett, JJ Tollett, and Randall G Hulet. Evidence of bose-einstein condensation in an atomic gas with attractive interactions. *Physical review letters*, 75(9):1687, 1995.

[82] Alexander L Fetter and Anatoly A Svidzinsky. Vortices in a trapped dilute bose-einstein condensate. *Journal of Physics: Condensed Matter*, 13(12):R135, 2001.

[83] Christopher J Pethick and Henrik Smith. *Bose-Einstein Condensation in Dilute Gases*. Cambridge University Press, 2002.

[84] Carlos Barcelo, Stefano Liberati, and Matt Visser. Analogue gravity from Bose-Einstein condensates. *Classical and Quantum Gravity*, 18(6):1137, 2001.

[85] Christian Cherubini and S Filippi. Boundary conditions for scattering problems from acoustic black holes. *Journal of the Korean Physical Society*, 56(51):1668–1672, 2010.

[86] F Federici, C Cherubini, S Succi, and MP Tosi. Superradiance from hydrodynamic vortices: A numerical study. *Physical Review A*, 73(3):033604, 2006.

[87] Lene Vestergaard Hau, Stephen E Harris, Zachary Dutton, and Cyrus H Behroozi. Light speed reduction to 17 metres per second in an ultracold atomic gas. *Nature*, 397(6720):594, 1999.

[88] Michael Robin Matthews, Brian P Anderson, PC Haljan, DS Hall, CE Wieman, and Eric A Cornell. Vortices in a bose-einstein condensate. *Physical Review Letters*, 83(13):2498, 1999.

[89] KW Madison, F Chevy, W Wohlleben, and Jl Dalibard. Vortex formation in a stirred bose-einstein condensate. *Physical review letters*, 84(5):806, 2000.

[90] Kevin C Wright, RB Blakestad, CJ Lobb, WD Phillips, and GK Campbell. Driving phase slips in a superfluid atom circuit with a rotating weak link. *Physical review letters*, 110(2):025302, 2013.

[91] Woo Jin Kwon, Joon Hyun Kim, Sang Won Seo, and Yong-il Shin. Observation of von kármán vortex street in an atomic superfluid gas. *Physical review letters*, 117(24):245301, 2016.

[92] AE Leanhardt, A Görlitz, AP Chikkatur, D Kielpinski, Y-i Shin, DE Pritchard, and W Ketterle. Imprinting vortices in a bose-einstein condensate using topological phases. *Physical review letters*, 89(19):190403, 2002.

[93] MF Andersen, Changhyun Ryu, Pierre Cladé, Vasant Natarajan, A Vaziri, Kristian Helmerson, and William D Phillips. Quantized rotation of atoms from photons with orbital angular momentum. *Physical review letters*, 97(17):170406, 2006.

[94] David R Scherer, Chad N Weiler, Tyler W Neely, and Brian P Anderson. Vortex formation by merging of multiple trapped bose-einstein condensates. *Physical review letters*, 98(11):110402, 2007.

[95] Chad N Weiler, Tyler W Neely, David R Scherer, Ashton S Bradley, Matthew J Davis, and Brian P Anderson. Spontaneous vortices in the formation of bose–einstein condensates. *Nature*, 455(7215):948, 2008.

[96] Simone Donadello, Simone Serafini, Tom Bienaimé, Franco Dalfovo, Giacomo Lamporesi, and Gabriele Ferrari. Creation and counting of defects in a temperature-quenched bose-einstein condensate. *Physical Review A*, 94(2):023628, 2016.

[97] Brian P Anderson, PC Haljan, Carl E Wieman, and Eric A Cornell. Vortex

precession in bose-einstein condensates: Observations with filled and empty cores. *Physical review letters*, 85(14):2857, 2000.

[98] E Hodby, G Hechenblaikner, SA Hopkins, OM Marago, and CJ Foot. Vortex nucleation in bose-einstein condensates in an oblate, purely magnetic potential. *Physical review letters*, 88(1):010405, 2001.

[99] C Raman, JR Abo-Shaeer, JM Vogels, K Xu, and W Ketterle. Vortex nucleation in a stirred bose-einstein condensate. *Physical review letters*, 87(21):210402, 2001.

[100] S Inouye, S Gupta, T Rosenband, AP Chikkatur, A Görlitz, TL Gustavson, AE Leanhardt, DE Pritchard, and W Ketterle. Observation of vortex phase singularities in bose-einstein condensates. *Physical Review Letters*, 87(8):080402, 2001.

[101] BP Anderson, PC Haljan, CA Regal, DL Feder, LA Collins, Charles W Clark, and Eric A Cornell. Watching dark solitons decay into vortex rings in a bose-einstein condensate. *Physical Review Letters*, 86(14):2926, 2001.

[102] Anton S Desyatnikov, Lluis Torner, and Yuri S Kivshar. Optical vortices and vortex solitons. *arXiv preprint nlin/0501026*, 2005.

[103] Yanzhi Zhang, Weizhu Bao, and Qiang Du. Numerical simulation of vortex dynamics in ginzburg-landau-schrödinger equation. *European Journal of Applied Mathematics*, 18(5):607–630, 2007.

[104] T R Slatyer and C M Savage. Superradiant scattering from a hydrodynamic vortex. *Classical and Quantum Gravity*, 22(19):3833, 2005.

[105] Franco Dalfovo, Stefano Giorgini, Lev P Pitaevskii, and Sandro Stringari. Theory of bose-einstein condensation in trapped gases. *Reviews of Modern Physics*, 71(3):463, 1999.

[106] R. Penrose. Gravitational collapse: The role of general relativity. *Nuovo Cimento 1 252*, 1969.

[107] Richard Brito, Vitor Cardoso, and Paolo Pani. Superradiance. *Lect. Notes Phys*, 906(1):1501–06570, 2015.

[108] Mauricio Richartz, Silke Weinfurtner, A. J. Penner, and W. G. Unruh. Generalized superradiant scattering. *Phys. Rev. D*, 80:124016, Dec 2009.

[109] Jacob D. Bekenstein and Marcelo Schiffer. The many faces of superradiance. *Phys. Rev. D*, 58:064014, Aug 1998.

[110] Alexei A. Starobinskil and S. M. Churilov. Amplification of electromagnetic and gravitational waves scattered by a rotating "black hole". *Sov. Phys. JETP*, 65(1):1–5, 1974.

[111] Ya B Zel'Dovich. Amplification of cylindrical electromagnetic waves reflected from a rotating body. *Soviet Physics-JETP 35 : 1085-1087.*, (1972).

[112] Mark A Scheel, Adrienne L Erickcek, Lior M Burko, Lawrence E Kidder, Harald P Pfeiffer, and Saul A Teukolsky. 3d simulations of linearized scalar fields in kerr spacetime. *Physical Review D*, 69(10):104006, 2004.

[113] C Cherubini, F Federici, S Succi, and MP Tosi. Excised acoustic black holes: The scattering problem in the time domain. *Physical Review D*, 72(8):084016, 2005.

[114] Nils Andersson, Pablo Laguna, and Philippos Papadopoulos. Dynamics of scalar fields in the background of rotating black holes. ii. a note on superradiance. *Phys. Rev. D*, 58:087503, Sep 1998.

[115] Miguel Alcubierre and Bernd Brügmann. Simple excision of a black hole in 3+1 numerical relativity. *Phys. Rev. D*, 63:104006, Apr 2001.

[116] K. Choy, T. Kruk, M. E. Carrington, T. Fugleberg, J. Zahn, R. Kobes, G. Kunstatter, and D. Pickering. Energy flow in acoustic black holes. *Phys. Rev. D*, 73:104011, May 2006.

[117] Emanuele Berti, Vitor Cardoso, and José P. S. Lemos. Quasinormal modes and classical wave propagation in analogue black holes. *Phys. Rev. D*, 70:124006, Dec 2004.